ABSTRACT

Title of Thesis:	DEVELOPMENT AND VALIDATION OF A PYROLYSIS MODEL FOR FLEXIBLE POLYURETHANE FOAM
	Siriwipa Kamma, Master of Science, 2024
Thesis Directed By:	Professor Stanislav I. Stoliarov, Fire Protection Engineering

Flexible polyurethane foam (FPUF) is a common material contained in household goods such as upholstered furniture and mattresses, which are known to significantly contribute to fire growth. An accurate prediction of fire development on FPUF containing items requires knowledge of FPUF pyrolysis and combustion properties. These properties include reaction kinetic parameters, thermodynamic parameters, and thermal transport properties. While many past studies focused on the thermal decomposing mechanism and thermodynamic properties of the reactions, the thermal transport properties have not been determined. In this study, a complete pyrolysis model of FPUF was developed by extending the thermal decomposition model from a previous study. The thermal transport properties were obtained using inverse modeling of the Controlled Atmosphere Pyrolysis Apparatus II experimental data. The complete model was validated against cone calorimetry data and found to perform in an adequate manner.

DEVELOPMENT AND VALIDATION OF A PYROLYSIS MODEL OF FLEXIBLE POLYURETHANE FOAM

by

Siriwipa Kamma

Thesis submitted to the Faculty of the Graduate School of the
University of Maryland, College Park, in partial fulfillment
of the requirements for the degree of
Master of Science
2024

Advisory Committee:
Professor Stanislav I. Stoliarov, Chair
Professor James A. Milke
Professor Shuna Ni

Acknowledgments

I remember watching American movies as a little girl dreaming that one day I would go to school there. It was not just a dream; it became reality. I am so lucky to have been born into a family that is not only supportive but also caring and understanding. I could not make it here without them. A special thank goes to my dad, who always supports and encourages me during difficult times.

Besides my family, the most significant acknowledgment goes to Dr. Stanislav Stoliarov. I am so grateful for the opportunity I have had to work with you. Your work has fascinated me in many aspects, especially your work ethic. You guided me throughout the process and showed me how to conduct good research. Your constructive advice helped to solve any problems that came along the way. Lastly, you have inspired me to continue conducting good work.

Thank you to my research group and other FPE graduate students for both help and friendship. Thanks to Sangkyu for helping me start my research, especially for staying with me while I was first running CAPA tests and going through the troubleshooting process with me; Farnaz for being so supportive, kind, and sharing research knowledge with me; Will for sharing your previous work, which made my research easier to understand.

Thank you to friends outside school who have been supportive and loving. Your encouragement helped me get through the hardships in classes and research. Special thanks to Jose, you have always believed in me.

Thank you to my thesis defense committee members, Dr. James Milke and Dr. Shuna Ni, for your valuable time. Thank you to the lab manager, Farid, for helping me

run tests until the last minute. Finally, I would like to thank the National Standard Institute of Technology for the financial support through grant 60NANB19D148.

Table of Contents

List of Tables

List of Figures

List of Abbreviations

HRR	-	Heat release rate
HOC	-	Heat of combustion
MLR	-	Mass Loss Rate (kg $s^{-1}m^{-2}$)
T_{bottom}	-	Bottom surface temperature (K)
A	-	Pre-exponential factor (s^{-1})
E_a	-	Activation energy (kJ mol^{-1})
c_p	-	Heat capacity (J kg^{-1} K^{-1})
ΔH_r	-	Heat reaction (J kg^{-1})
ΔH_c	-	Heat of combustion (J kg^{-1})
$q_{r,top}$	-	Top boundary radiative heat flux (W m^{-2})
$q_{c,top}$	-	Top boundary convective heat flux (W m^{-2})
$T_{gas,top}$	-	Top surface environmental temperature (K)
$h_{c,top}$	-	Top boundary convective heat transfer (W $m^{-2}K$)
$q_{r,bottom}$	-	Bottom boundary radiative heat flux (W m^{-2})
$q_{c,bottom}$	-	Bottom boundary convective heat flux (W m^{-2})
$h_{c,bottom}$	-	Convective heat transfer coefficient of the bottom surface (W $m^{-2}K$)
ε	-	Emissivity
σ	-	Stefan-Boltzmann constant, 5.67×10^{-8} W $m^{-2}K^{-4}$
α	-	Absorption coefficient (m^2 kg^{-1})
k_{FPUF}	-	Thermal conductivity of virgin FPUF (W $m^{-1}K^{-1}$)

k_{prod}	-	Thermal conductivity of condensed-phase decomposition products (W $m^{-1}K^{-1}$)
k_{gas}	-	Thermal conductivity of gaseous decomposition products (W $m^{-1}K^{-1}$)
MLR_{err}	-	Mass loss rate optimized error
$T_{b,err}$	-	Bottom surface temperature optimized error
$\overline{MLR}$	-	Average MLR (kg $s^{-1}m^{-2}$)
c_x	-	Effective absorption coefficient (m^2s kg^{-1})
$q_{r,cone}$	-	Front boundary radiative heat flux of cone calorimeter (W m^{-2})
MLRPUA	-	Mass loss rate per unit area of cone calorimeter (kg $s^{-1}m^{-2}$)
HRRPUA	-	Heat release rate per unit area of cone calorimeter (kW m^{-2})

Chapter 1: Introduction

1.1 Motivation

The leading cause of fatalities in U.S. home structure fires is the presence of aesthetic household items like upholstered furniture and mattresses [1]. According to the National Fire Protection Association (NFPA) [2], between 2015 and 2019, an annual average of 2,620 deaths occurred due to home structure fires, with 410 deaths (16 %) attributed to upholstered furniture and 320 deaths (12%) to mattresses or bedding as the first items to ignite. This shocking data reveals that nearly 30% of these annual deaths are caused by these household goods alone. As these items have become more integral to modern homes, the fire risks and losses associated with them have escalated significantly.

Under layers of fabric, flexible polyurethane foam (FPUF) is a common material that is filled in upholstered furniture and mattresses because of its comfort, support, and durability benefits [3]. However, FPUF is an extremely flammable material in the fire environment. When exposed to a heat source, it ignites quickly and then collapses into a flaming liquid pool [4], allowing the fire to spread easily. The fire risks associated with FPUF are significant even when it is not the first item to ignite. From a fire safety perspective, it is clear that FPUF poses a serious threat to many lives. Therefore, understanding the flammability of this highly flammable material is crucial.

Many studies have focused on FPUF since 1970 [4]. Several standard tests have been implemented for both smoldering and flaming combustions, such as California Technical Bulletin (TB-117) [5], which is a standard smoldering (cigarette) ignition

test for upholstered furniture, and the 16 Code of Federal Regulations (C.F.R.) test # 1632 [6] and #1633 [7], which are standard tests for mattresses and bedding using smoldering (cigarette) and open flame ignition sources, respectively. Additionally, several passive fire protection approaches, such as fabric barriers [8] and fire retardant (FR) additives [9], have been studied to help slow down the ignition of FPUF [4].

Numerous standard tests and passive fire protection methods have been established to replicate real fire scenarios. These tests usually incur substantial costs and require significant time. Alternatively, computational fire modeling can represent many fire scenarios in a timely and cost-effective manner. Fire modeling consists of gas-phase computational fluid dynamics (CFD) and condensed-phase pyrolysis solvers. While the physics of gas-phase CFD solvers have been extensively developed in areas such as combustion, fluid flow, and heat transfer, condensed-phase pyrolysis solvers that require pyrolysis property sets, commonly referred to as 'pyrolysis models', of any combustible materials of interest have not yet been widely developed. The pyrolysis models are essential components for pyrolysis solvers to accurately predict flame spread and fire growth in fire scenarios [10]. Further research into condensed-phase pyrolysis models for various materials, including FPUF, is necessary to improve fire simulation results.

1.2 Background

1.2.1 Pyrolysis Modeling Development

In a typical fire scenario, when a heat source is near the material, the material begins to decompose over time and at sufficient temperatures, producing volatile

gaseous products. This thermal decomposition process is known as pyrolysis. With an ignition source, the gaseous pyrolyzates combust with available oxygen in the surrounding environment, releasing energy in the form of heat and light, known as fire. This high energy of fire then provides heat feedback to decompose more material, continuing to produce more gaseous fuel and sustaining the combustion reaction until there is no more material to decompose. The purpose of the fire simulation is to accurately replicate this scenario. As previously mentioned, the fire computational simulation includes two complex solvers: gas-phased CFD and condensed-phase pyrolysis solvers as demonstrated in Figure 1.1. The gas-phased CFD solver predicts the combustion reactions of gases in space, while the condensed-phase pyrolysis solver focuses on the thermal decomposition of solid or liquid materials into volatile gaseous products. The ultimate goal of the pyrolysis solver is to precisely predict the rate of gasification based on the physical and chemical properties of the pyrolyzed material.

Figure 1.1. Computational fire modeling components.

Several pyrolysis solvers have been developed since the 1980s [7, 8]. Common pyrolysis solvers include Gpyro [9, 10], Solid-Phase solver within Fire Dynamics Simulator (FDS) [15], and ThermaKin [12, 13]. These solvers are capable of solving transient energy transfer, both radiative and conductive, coupled with decomposition

chemistry in a comparable manner. They not only share similar solving capabilities but also require similar inputs, including decomposition reaction kinetic parameters, thermodynamic parameters, as well as, thermal transport properties. This completed set of inputs is referred to as a 'pyrolysis model'.

This study aims to develop a complete pyrolysis model of FPUF following a hierarchical approach [10]. This approach relies on experimental results of milligram-sized and gram-sized material samples using inverse modeling analysis. The milligram-sized samples are performed using thermogravimetric analysis (TGA), differential scanning calorimeter (DSC), and microscale combustion calorimeter (MCC) to determine thermal decomposition mechanism, kinetic parameters, heat capacities of condensed-phase components, heat decomposition reactions, and heat of combustions of gaseous pyrolyzates. The gram-sized samples are performed using a Controlled Atmosphere Pyrolysis Apparatus II (CAPA II) to determine the thermal transport properties and complete the pyrolysis model. Once all parameters are defined, the complete pyrolysis model can be generated to accurately simulate and predict the behavior of FPUF undergoing the thermal decomposition process.

1.2.2 Review Previous FPUF Pyrolysis Studies

Pyrolysis is the thermal decomposition process of a material exposed to a heat source. It is an initial mechanism in the solid or liquid combustion process. For a porous material like FPUF, two types of combustion typically occur: flaming and smoldering combustion. Figure 1.2 demonstrates the different types of combustion during the pyrolysis process of solid fuels. Flaming combustion happens when the solid undergoes pyrolysis in the absence of oxygen near the pyrolyzed surface. The presence of a flame

consumes oxygen from the surrounding atmosphere, blocking oxygen from reaching resulting in anaerobic combustion. On the other hand, smoldering combustion occurs at a low temperature in the absence of flame [18] allowing oxygen to interact with the pyrolyzed surface. The type of combustion happens in an aerobic atmosphere at a relatively slow rate but can serve as an initiating source of flaming combustion.

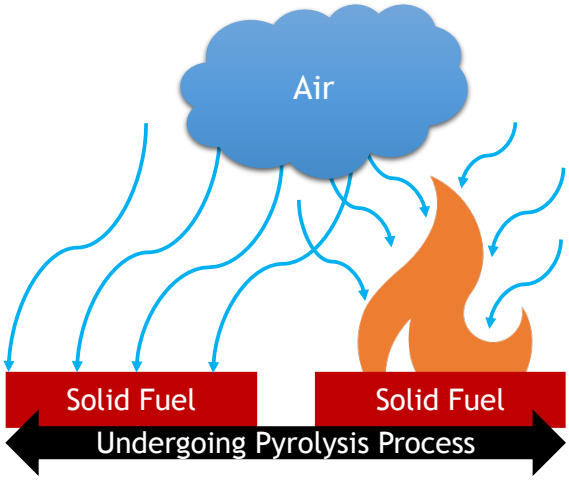

Figure 1.2. Flaming (right) vs. smoldering (left) combustion of pyrolyzing solid fuels.

Pau et al. [19] performed the TGA experiments at heating rate from 1 – 60 °C min^{-1} on both FR and non-fire retardant (NFR) polyurethane (PU) foam under an anaerobic atmosphere using two reaction schemes; then, inversely analyzed the data using three different graphical techniques: kinetic analysis, Arrhenius plot methods, and inflection point methods, instead of using a computational model method to compare their effects on kinetic parameters A, E, and n (for the Arrhenius plot and inflection point method only). The kinetic parameters obtained can be used with Gpyro, and pyrolysis model in FDS version 5. It was found that the kinetic properties of PU foam obtained through different calculation techniques were consistent within the same techniques but showed increasing derivation at extreme heating rates and for properties

with higher magnitudes. The overall trend in each technique for the first and second reactions was also consistent: A and E of the second reaction were higher in magnitude than the first reaction, and n of the second reaction was smaller in magnitude than the first reaction. Garrido and Font [20] performed TGA experiments on FPUF in three atmospheres to obtain kinetic models for pyrolysis (anaerobic atmosphere) and combustion (aerobic atmosphere). The anaerobic kinetic model was consistent with 2-consecutive reactions, while 3-consecutive reactions were observed in the aerobic atmosphere. Also, the sample was characterized using TG-IR and TG-MS in both atmospheres. In an anaerobic atmosphere, the foam began to break urethane bonds in the first reaction, and then immediately degraded. In the aerobic atmosphere, the foam broke the urethan bonds in the first reaction, and some of the ether polyols began to degrade, finishing in the second reaction and creating char in the last reaction. Prasad et al. [21] coupled gas-phase and condensed-phase solvers to enhance the flame spread model of a 10-cm thick FPUF. The properties of the foam during decomposition were estimated from various small-scale experiments. TGA and DSC were used to analyze the decomposition and the heat of reaction, MCC was used to determine the heat release (HR) of reactions, and the cone calorimeter was used to measure HRR and mass loss at different heat fluxes. The data obtained from these small-scale experiments were used to develop models, but temperature-dependent conductivity and specific heat of condensed-phase components were assigned from the literature along with optical properties such as emissivity and absorption coefficient. The developed model was simulated in FDS to predict the flame spread rate, HRR, and heat flux of large-scale

experiments. While the model qualitatively captured the observed trends in the large-scale tests, it was not completely accurate when compared with the experimental data.

1.3 Objective and Research Approach

A complete pyrolysis property that includes decomposition reaction kinetic parameters, thermodynamics parameters, and thermal transport properties of FPUF is not currently unavailable. The primary goal of this study was to develop a complete pyrolysis property set, commonly referred to as the pyrolysis model, of NIST standard FPUF in an anaerobic atmosphere. This study aimed to extend the thermal decomposition model of NIST standard FPUF developed by Saar [22].

By following the hierarchical approach [10], Saar [22] accurately determined the decomposition reaction kinetic parameters and thermodynamic parameters from milligram-sized samples (details can be found in section 4.1). In this study, CAPA II experiments using gram-sized samples in an anaerobic atmosphere were performed to obtain transport properties of reaction components of NIST standard FPUF. Additionally, CAPA II experiments in an aerobic atmosphere are conducted to observe the foam's behavior in the presence of oxygen. Once the complete pyrolysis model is obtained, the cone calorimeter [23] experiments were performed to acquire the heat release rate (HRR), and heat of combustion (HOC). Furthermore, the complete pyrolysis model was validated using cone calorimetry experimental data to ensure its accuracy and performance in both anaerobic gasification and flaming combustion scenarios. ThermaKin2Ds [17] pyrolysis solver was utilized as the pyrolysis solver throughout this study.

Chapter 2: Methodology

2.1 Material

Flexible polyurethane foam is typically formed by mixing polyol and isocyanate with water and other additives [3]. The formulations of FPUF vary depending on the additives, which make each foam distinct. For all experiments performed in this study, NIST standard FPUF, an open-cell, polyether-based foam compliant with TB-117-2013 [5], was utilized. The foam was made from a mixture of polyols, including propylene oxide and ethylene oxide polyols, and diisocyanate (TDI), consisting of 80% 2,4-TDI and 20% 2,6-TDI, and had no fire retardant or post-product fire retardant treatment [5]. The density of the foam was measured to be 29.4 ± 0.3 kg m-3.

2.2 Experimental Methods

2.2.1 CAPA II

CAPA II is a gasification apparatus that provides well-defined thermal boundary conditions and highly resolved simultaneous measurement of mass, temperature, and profile evolution of a 70 mm diameter disk-shaped sample [24]. This apparatus enables an extensive evaluation of controlled pyrolysis of charring and intumescent material. It also allows the prediction of thermal conductivity through inversed analysis of measurement data. Figures 2.1 and 2.2 show the drawings of CAPA II.

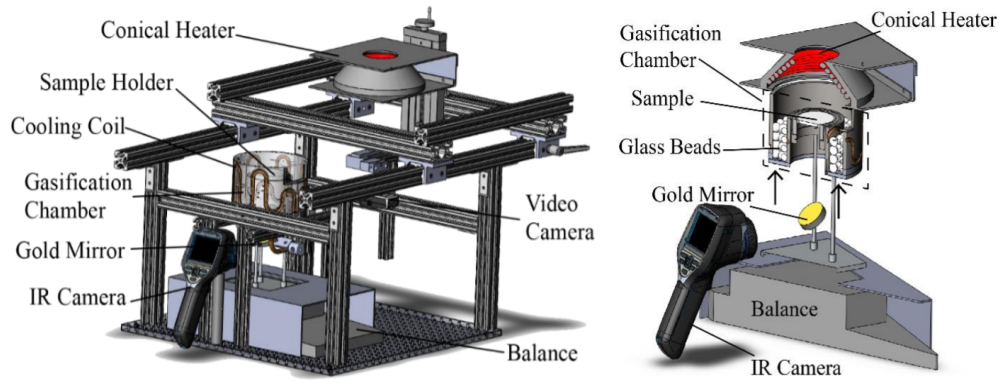

Figure 2.1. Three-dimensional drawing of CAPA II.

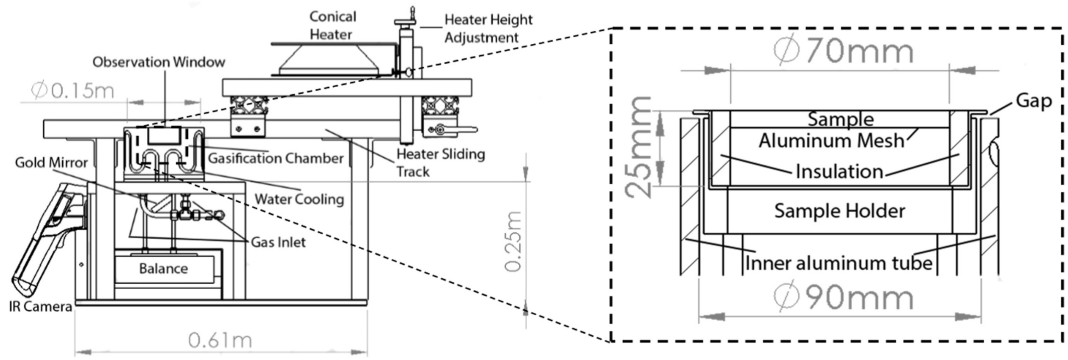

Figure 2.2. Schematic drawing of CAPA II with its sample holder detailing.

CAPA II mainly consists of an electric radiant conical heater, a gasification chamber, an infrared camera, a mass balance, and a video camera. The electric radiant conical heater, which can provide up to 100 kW m^{-2} heat flux, is mounted on a sliding track that allows it to be quickly positioned above the gasification chamber and removed from it. An open-to-the-atmosphere gasification chamber, which is water-cooled, is assembled of two concentric aluminum tubes, each 6.4 mm thick. In Figure 2.2, the inside of the inner tube contains a steel sample holder. The initial sample surface is leveled with the sample holder lip, which extends to cover the gap between the holder and the inner tube, diminishing air entrainment from beneath the sample. The outer tube is designed to be 0.01 m below the bottom of the conical heater housing

and 0.03 m above the sample surface, minimizing air entrainment from the open-to-the-atmosphere top. A small section of the outer tube is replaced with quartz to create an observation window, allowing visual observation during experiments. The inner wall of the outer tube is coated with high-emissivity paint to suppress radiant heat from the conical heater. To cool the chamber, copper tubes are inserted into cutting channels on the exterior wall of both tubes, enabling water to circulate constantly. The channel between the two tubes is filled with layers of 6.4 mm diameter glass beads to create a uniform flow of purged gas, which will constantly flow to maintain the sample surface atmosphere. The gas composition can be described.

The three primary diagnostics of CAPA II include mass, bottom surface temperature (T_{bottom}), and sample surface profile. During the experiment, instantaneous mass is recorded using high precision (1 mg) Sartorius Cubis balance at 2 Hz frequency. T_{bottom} is recorded by a FLIR E40 infrared (IR) camera at a 7.5 Hz frequency. Due to the geometrical constraint of the apparatus, the IR camera cannot directly record T_{bottom}. Instead, it is focused on the gold mirror with an average reflectance of 0.96, which reflects a thin copper foil on the bottom of the sample. The copper foil is coated with a high emissivity paint of 0.92. The IR camera's emissivity is adjusted for transmission loss through the gold mirror and validated using thermocouple-based temperature measurements. The sample surface profile is recorded using a Logitech C930e high-definition camera through the quartz observation window. Additionally, two 1.3 mm Type K thermocouples, each attached to the wall of the inner and outer aluminum tubes, are used to monitor the sample's atmospheric temperatures.

CAPA II is typically designed for samples with a diameter ranging from 30 - 70 mm and thickness from 1 – 20 mm. Kaowool PM insulation board that is cut into rings is used to thermally insulate the sample holder and the perimeter of the sample, as detailed in Figure 2.2. The cylindrical sample holder has a diameter of 82 mm and a depth of 25 mm. The bottom of the sample holder has a 70 mm hole that reveals the bottom surface of the sample to the gold mirror. The 12 mm thick ring at the bottom lip of the sample holder acts as a shelf for layers of Kaowool PM rings. A diamond-shaped aluminum mesh, 0.76 mm thick and coated with high emissivity paint ($\varepsilon = 0.92$), is placed between the Kaowool PM rings at the desired height. This circular cut mesh that is covered with painted copper foil helps support the bottom of the sample and prevents air entrainment beneath the sample. However, the decomposition characteristics of FPUF significantly differ from materials previously studied on CAPA II [24 - 29]. Specific sample preparation approaches were developed to accommodate the uniqueness of the physical characteristics of FPUF during its decomposition process in CAPA II experiments.

FPUF is known as a low-density material, with a density of about 50 – 100 times less than the typical materials studied [24 - 29] on CAPA II. This lightweight material caused an issue of undetectable mass loss due to balance signal noise during the decomposition process. In this study, FPUF samples were cut into disks with a diameter of 70 mm and a thickness of 20 mm. Once exposed to heat, the FPUF rapidly collapses, producing a liquid pool on the bottom of the holder. To address this, 12.7 mm wide Scotch 69 high-temperature insulation electrical tape was used between the lip and the copper foil to create a cup-liked structure at the bottom of the sample holder

during the experiments. The cup prevented any leakage of material during the decomposition process of FPUF. The sample holder preparation procedures are described in Appendix A1. In the experiment, the sample holders were pre-exposed to the radiant heater until no more mass loss was observed from the tape's adhesive. The conical heater was set to the desired heat flux using a water-cooled Schmidt-Boelter heat flux gauge at a setpoint level where the sample holder lip was leveled.

Due to the rapid collapse of FPUF, the heat flux delivered to the pool at the bottom of the sample holder was reduced from the setpoint flux. To minimize this effect, the samples were placed so that their top surface protruded 7 mm above the sample holder lip, leaving 13 mm of the sample thickness inside the sample holder. The reduced heat flux received by the pool was measured using another water-cooled Schmidt-Boelter heat flux gauge to quantify the reduction.

CAPA II experiments in this study were performed in both anaerobic and aerobic atmospheres. In the anaerobic atmosphere, a constant 185 SLPM of nitrogen was used as the purge gas flowing through the gasification chamber. Three different radiant heat fluxes that were measured at the setpoint level were selected for the FPUF sample: 26, 41, and 62 kW m^{-2}. For 26 and 41 kW m^{-2} heat flux exposures, five repeated experiments were conducted for each flux. For 62 kW m^{-2} flux, seven repeated experiments were conducted. In the aerobic atmosphere experiments, 185 SLPM of dry air was used as a purge gas under a radiant heat flux of 26 kW m-2. The repeated experiments were performed to ensure reproducibility and accumulate necessary statistics.

For all experiments performed on CAPA II, mass loss rate (MLR) was computed using a 4-second time differential and normalized by the initial top surface area of the sample. The mass data were subsequently grouped into 4-second bins, providing mean MLR and mean time in each bin. MLR and T_{bottom} data were grouped before averaging. The experiment began when the conical heater was slid into position over the gasification chamber and terminated when no mass loss was detectable on the balance.

2.2.2 Cone Calorimeter

Cone Calorimeter experiments were performed in accordance with ASTM E1354 [23]. The C-factor of the cone calorimeter was calibrated daily before the experiment. Calibration was performed on cast poly(methyl methacrylate) to ensure the heat of combustion (HOC) matched published values. FPUF samples were prepared as 10 × 10 cm squares and 2 cm thick. The bottom surface of each sample was wrapped with a thin aluminum foil, covering half of the sample thickness (1 cm) on all four sides. The aluminum-wrapped samples were placed on three layers of 6.4 mm thick and one layer of 3.2 mm Kaowool PM insulation boards, which were set on the sample holder. No retainer frame was used in the experiments. The aluminum foil helped prevent mass from flowing through the Kaowool PM insulation. A spark igniter that positioned 13 mm above the sample's top surface was used for ignition. Three experiments were performed at a set heat flux of 26 kW m^{-2} to accumulate statistics.

2.3 Modeling

ThermaKin2Ds, a comprehensive numerical pyrolysis solver [17], was used for all computational modeling in this study. This solver enabled quantitative prediction of various material behaviors in response to external heat, handling both anaerobic and aerobic pyrolysis separately from a gas-phased combustion solver [17]. It can perform one-dimensional and two-dimensional simulations in both Cartesian and cylindrical coordinates, solving transient energy and mass conservation equations for a condensed-phase object of any composition undergoing physical and chemical transformation.

The simulation of CAPA experiments was conducted using one-dimensional approximation, which was determined to be sufficient due to the nearly uniform radial distribution of T_{bottom} and sample thickness profile. Only anaerobic CAPA experiments were simulated in this study. The gas transport coefficient was set to be 2 $\times$ 10^{-5} m^2 s^{-1} for all gas decomposition products ensuring that the rate at which gases left the sample was equal to their production rate, with gas concentration inside the sample was negligible. The top surface of the sample was set to have no gas flow resistance, while gases could not flow through the bottom surface of the sample.

The integration parameters were set with an element size of 0.01 mm and a time step of 5 ms. The convergence of the numerical solutions was verified by comparing the model to the version that were increased time step by a factor of 2 and 4, showing no significant changes in the results.

The simulation of cone calorimeter modeling was used to validate the modeling of the pyrolysis model. The model was performed using a one-dimensional simulation. The integration parameters were set to be the same as those used in CAPA experiment

simulations. An empirical flame heat feedback model [31], developed for the standard cone calorimeter test, was implemented to define the boundary conditions of the sample's top surface. A single-zone flame model (as detailed in a previous study [31]) was chosen in this study to simplify the validation of the pyrolysis model. Kaowool PM insulation layers with known thermophysical properties [31] beneath the sample create an adiabatic condition on the sample's bottom surface.

Chapter 3: Experimental Results

3.1 CAPA II

3.1.1 Nitrogen Atmosphere

Average MLR results of each flux exposure were calculated using 4-seconds time differential and presented with an uncertainty calculated as 2 standard deviations of the scatter data. On the other hand, the average T_{bottom} results were illustrated with uncertainty using 2 standard deviations of the mean temperature from each experiment, instead of the scatter data from all experiments. This mean temperature uncertainty helped to capture the variability of the T_{bottom} profiles between experiments. A mass fraction was defined as the difference between an average initial mass among all samples in the same heat flux exposure and an average instantaneous total mass loss normalized by the average initial mass, and the results were plotted concurrently with the average MLR results. During the experiment with extremely lightweight FPUF in a high-temperature environment, the instantaneous mass recorded was lower than the actual mass, resulting in higher MLR. A correction coefficient of 0.94 was applied to the average MLR results for all heat flux exposures to adjust the mass loss data. The coefficient was verified by matching the residual mass fraction to the experiments with the integrated average MLR. There was some residual left after the experiment of 26 kW m^{-2}, but no residual mass left after the experiment of 41 kW m^{-2} and 62 kW m^{-2} heat flux exposure. The MLR with mass fraction results are shown in Figure 3.1. T_{bottom} results are shown in Figure 3.2.

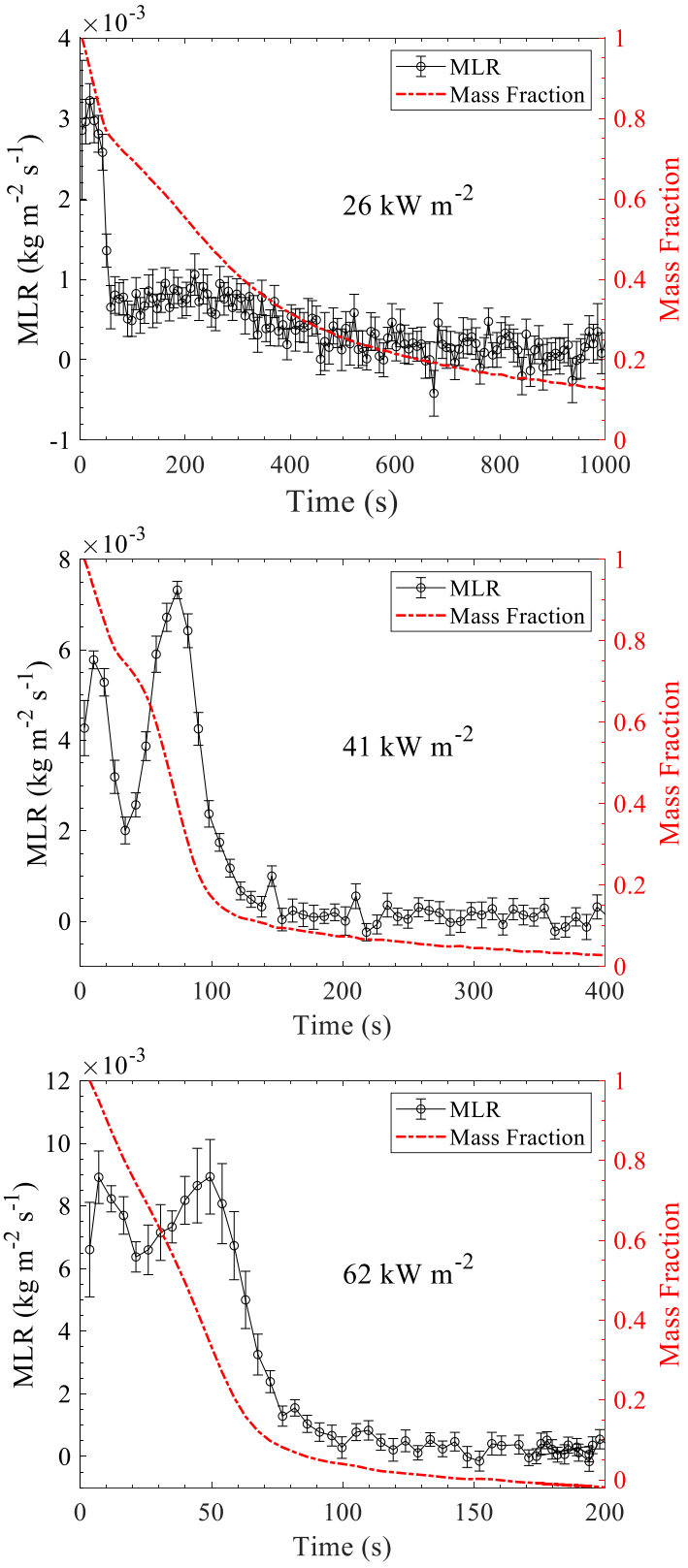

Figure 3.1. Average MLR with mass fraction from CAPA II experiments at all heat flux exposure.

The MLR of each heat flux exposure results demonstrate distinctive behaviors. At 26 kW m^{-2}, the first sharp MLR peak is observed at 18 seconds, then rapidly decays within 40 seconds. A smaller peak appears around 220 seconds, and by about 550 seconds, the MLR slowly declines to a steady low level near zero for the rest of the experiment. At 41 kW m^{-2}, two sharp MLR peaks are observed: one at around 10 s. with a 14-second decay, and another at around 74 seconds with an 80-second decay, followed by a constant mass loss near zero for the rest of the duration.

At 62 kW m^{-2} exposure, 2 sharp peak MLRs are also observed, but both of the peaks are almost equal in magnitude. The first peak occurs at 7 s with about 14 s decay, and the second peak is at 49 s with about 50 s decay, followed by a constant mass loss rate near- zero rate until the experiment ends.

Figure 3.2 shows different T_{bottom} behavior of each heat flux exposure is observed. At 26 kW m^{-2}, the peak temperature occurs around 185 s, then slowly declines and remains almost for the rest of the experiment. At 41 kW m^{-2}, the peak T_{bottom} is at 90 s, then declines for about 100 s. After 200 s, T_{bottom} slowly declines for the rest of the experiment. At 62 kW m^{-2}, an unusual T_{bottom} behavior is observed. The peak T_{bottom} occurs at 50 s and then declines for about 13 s. After that, T_{bottom} slightly rises and stays constant for about 50 s. Around 130 s, the T_{bottom} slowly declines for the rest of the experiment. It is important to note that the higher heat flux exposure results in higher T_{bottom} values.

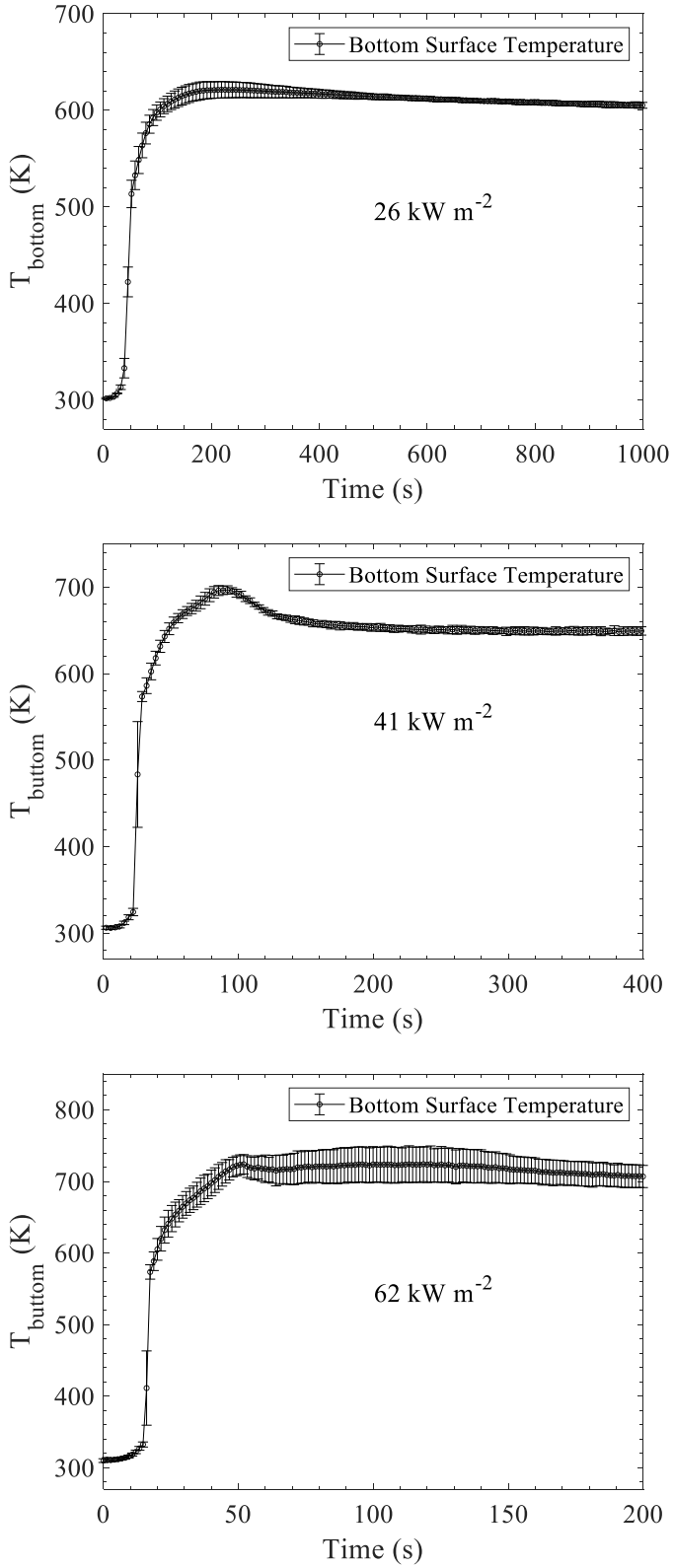

Figure 3.2. Average bottom surface temperature from CAPA II experiments at all heat flux exposure.

In addition to MLR and T_{bottom} results, the physical decomposition of FPUF during CAPA II experiments was observed. The sample thickness profile of each heat flux exposure, along with their physical decomposition are shown in Figure 3.3 – 3.5.

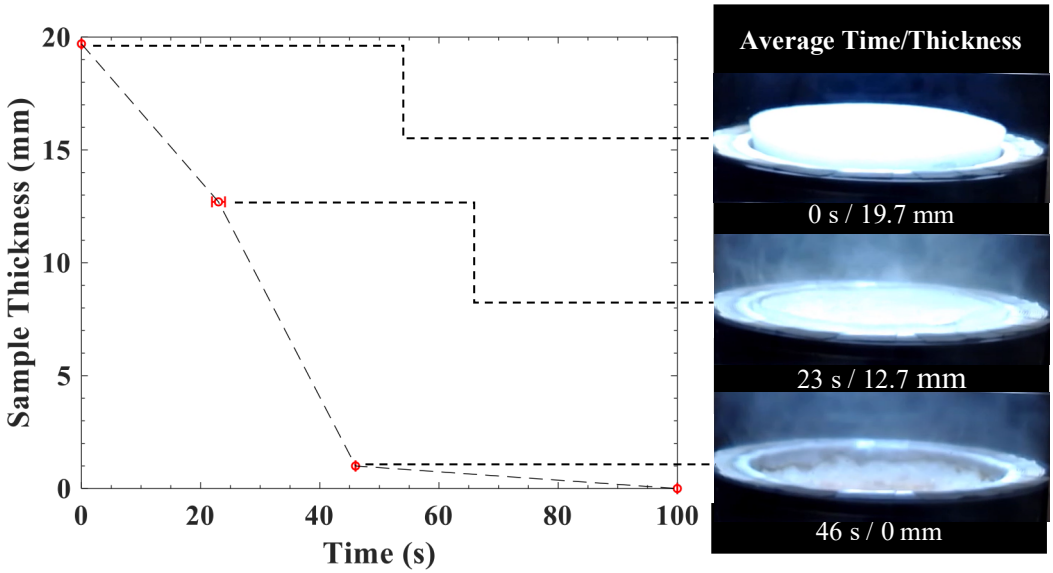

Figure 3.3. Sample Thickness profile (left) with its physical decomposition behavior (right) of 26 kW m^{-2} of CAPA II experiments.

For 26 kW m^{-2} exposure, samples collapsed to the sample holder lip within 23 s, then fully collapsed into a shallow pool with an approximate remaining thickness of 1 mm at 46 s, which was relatively quick. During the collapse, bubbles formed on the foam's top surface. The pool then gradually decomposed into volatile gas with a bubbly surface for the remaining duration. A similar physical decomposition behavior was observed for 41 and 62 kW m^{-2} heat flux exposures, as shown in Figure 3.4 for 41 kW m^{-2} and Figure 3.5 for 62 kW m^{-2}. Samples collapsed to the lip of the sample holder at 9.7 s and 4.2 s for 41 and 62 kW m^{-2}, respectively. They then collapsed to about 1 mm thick pool at 22 s and 13.2 s for 41 and 62 kW m^{-2}, respectively, and slowly decomposed for the remainder of the experiments.

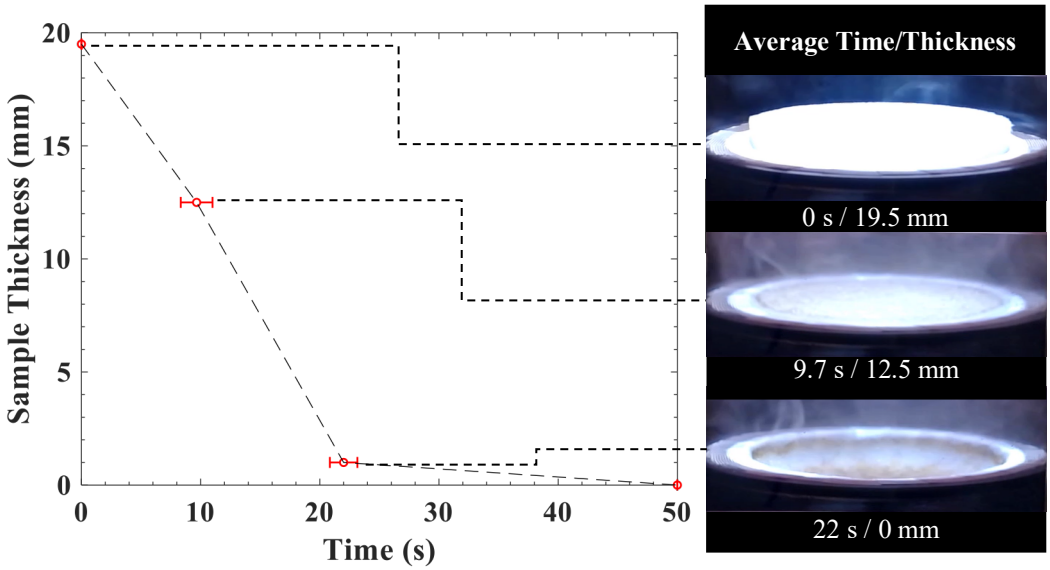

Figure 3.4. Sample Thickness profile (left) with its physical decomposition behavior (right) of 41 kW m^{-2} of CAPA II experiments.

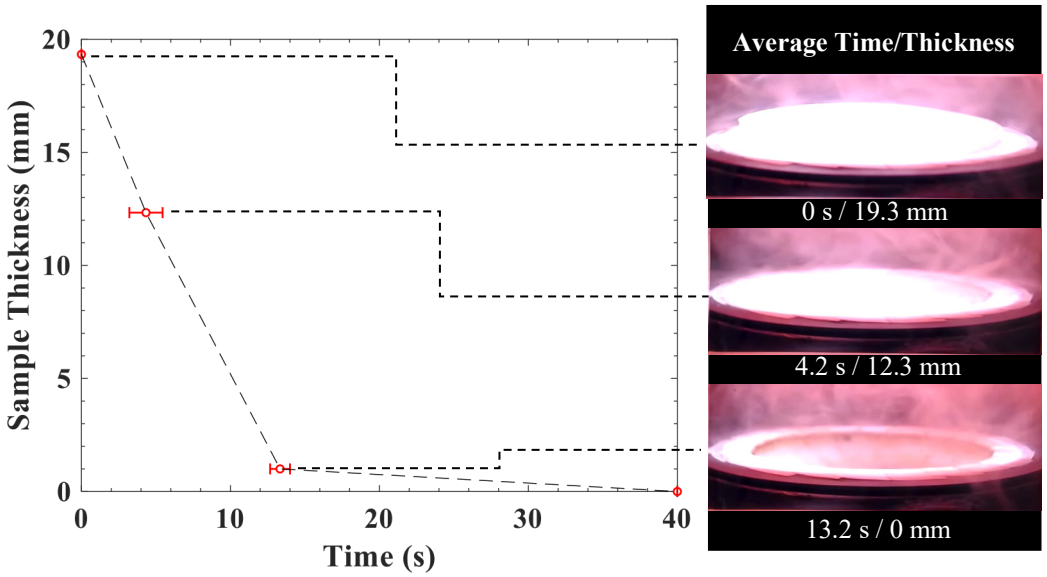

Figure 3.5. Sample Thickness profile (left) with its physical decomposition behavior (right) of 62 kW m^{-2} of CAPA II experiments.

3.1.2 Air Atmosphere

The CAPA aerobic atmosphere experiment was conducted to observe the behavior of FPUF in the presence of oxygen. When exposed to a low heat flux, 26 kW m^{-2}, no flame was observed in any of the experiments. The average MLR and T_{bottom} results from the CAPA II aerobic atmosphere experiments were analyzed using the same method as anaerobic atmosphere data. An MLR coefficient of 0.94 was also applied for consistency. The average MLR and T_{bottom} are plotted concurrently with 26 kW m^{-2} exposure CAPA II anaerobic atmosphere experiments, as shown in Figure 3.6 – 3.7.

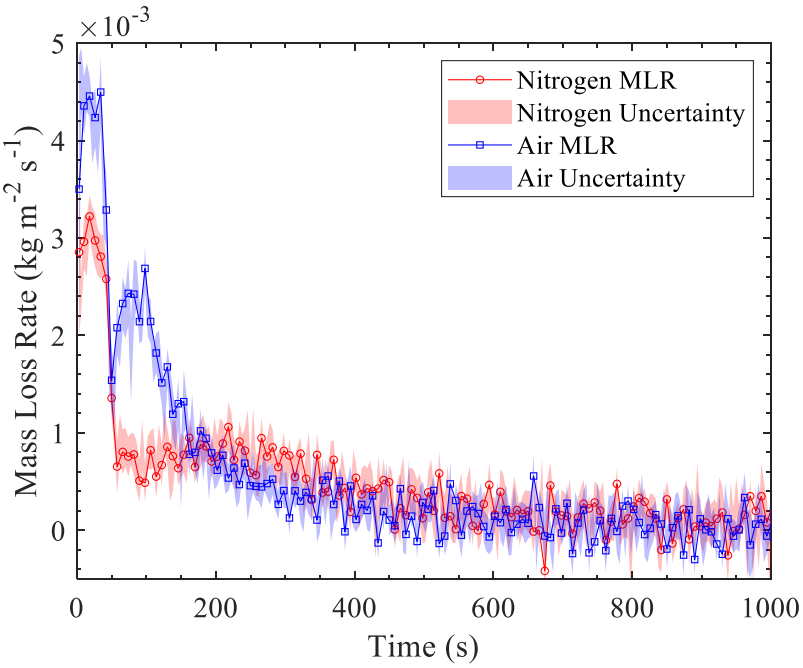

Figure 3.6. Average MLR of CAPA II experiments in both anaerobic and aerobic atmosphere at 26 kW m^{-2} heat flux exposure.

A comparison of the MLR collected in nitrogen and air shows a higher rate of mass loss in the presence of oxygen. The first sharp peak occurs at almost the same time as the anaerobic atmosphere but is about 50% higher in magnitude, then decays

within a similar period. The second peak of aerobic MLR occurs at around 100 s and decays over about 300 s to a steady, low value near zero. The second peak of aerobic MLR occurs earlier and at a higher rate (~150%) than the anaerobic MLR. Furthermore, the average T_{bottom} in an aerobic atmosphere shows similar behavior to that in an anaerobic atmosphere, but the peak T_{bottom} in the aerobic atmosphere is slightly higher (~20 K), as shown in Figure 3.7. Notably, the peak T_{bottom} occurs around 100 s, coinciding with the second peak of MLR in an aerobic atmosphere. These results indicate that the presence of oxygen in the environment contributes to a higher MLR and temperature of the material.

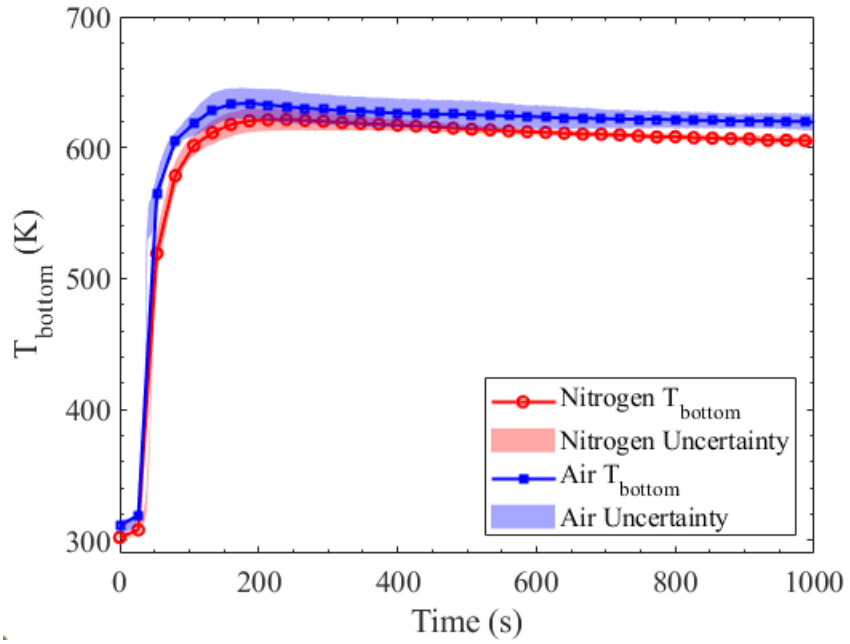

Figure 3.7. Average bottom surface temperature of CAPA II experiments both anaerobic and aerobic atmospheric at 26 kW m^{-2} heat flux exposure.

Besides MLR and T_{bottom}, the sample thickness profile in the aerobic atmosphere was also observed. The results are plotted concurrently with the anaerobic atmosphere exposure at the same heat flux, as shown in Figure 3.8. The thickness

profile exhibits distinctive behavior in the aerobic atmosphere. During exposure, the top surface of the sample oxidized, creating a charring layer. This charring layer trapped the decomposition of gaseous products beneath it, generating a balloon-like surface due to the high pressure underneath. Once the gaseous products were depressurized and released from the surface, they dropped to the pool level at the bottom of the sample holder while the pool continued decomposing and producing gases. The charring layer then turned to a solid residue sitting on top of the decomposition products, preventing gaseous pyrolyztes from flowing through the surface. The solid surface was lifted by the pressurized gases and then continued consistently for the rest of the experiments.

The overall comparison between anaerobic and aerobic atmospheres shows no significant difference in the decomposing behavior of FPUF in different environments. Therefore, this study will focus on the decomposition in the nitrogen (anaerobic) atmosphere.

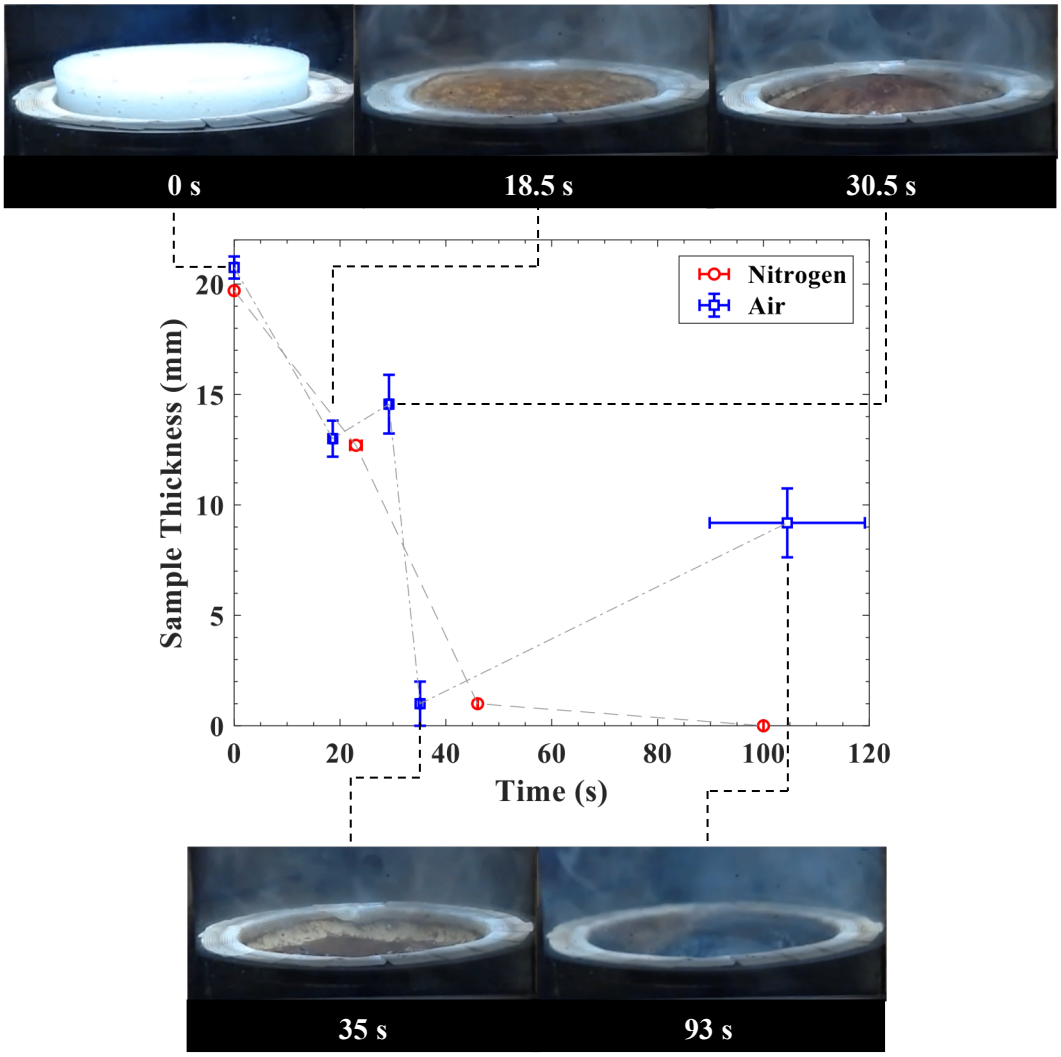

Figure 3.8. Sample thickness profile with its physical decomposition behavior of the aerobic atmospheric experiments comparing to sample thickness profile of the anaerobic atmospheric experiments CAPA II at 26 kW m^{-2} heat flux exposure.

3.2 Cone Calorimeter

FPUF samples were used to determine HOC when FPUF experienced complete combustion using a cone calorimeter in accordance with ASTM 1354 [23]. The average HRR of each experiment was normalized by the sample surface area to obtain the heat release rate per unit area (HRRPUA). Uncertainty was calculated using 2 standard

deviations of the mean HHRPUA of each test. The average HRRPUA is shown in Figure 3.9.

HOC was calculated as a ratio of the area under the HRR curve to the total mass loss. During the experiments, the calibration performed on cast poly(methyl methacrylate) provided a slightly lower HOC value than published values. Therefore, a correction factor, which was a ratio of the published value to the experimental value, was applied to adjust the HOC of FPUF. As a result, the average HOC was calculated to be 27.4 ± 1.5 kJ g^{-1}, which is within the range of the published values [32, 33]. Moreover, an average mass loss rate per unit area (MLRPUA) of the foam was calculated as the ratio of HRRPUA to HOC for each experiment, and then the average MLRPUA was determined.

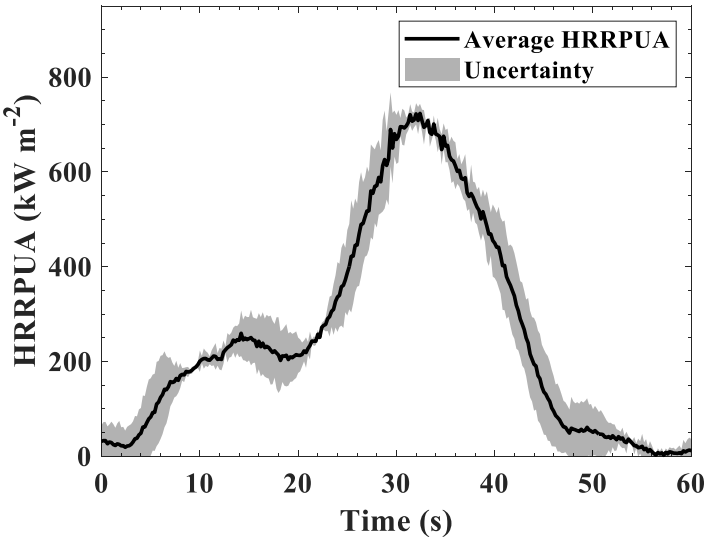

Figure 3.9. Average HRRPUA of cone calorimeter experiments.

Chapter 4: Modeling Framework and Results

4.1 Model Development

As previously mentioned, the pyrolysis model development in this study followed the hierarchical approach [10]. A prior study by Saar [22] on an FPUF decomposition model accurately determined kinetic parameters, thermodynamic parameters, and the heat combustion (ΔH_c) of gas-phase decomposition products by using the ThermaKin2Ds solver. The parameters developed in Saar's model, summarized in section 4.1.1, were used to complete the FPUF pyrolysis model by determining heat and mass transport properties from CAPA experimental data and then validating the complete model with the cone calorimeter experimental data.

4.1.1 Previous Study Parameters

By using NIST standard FPUF, Saar [22] defined the thermal decomposition of FPUF as 2- consecutive first-order reactions:

$$(1) \qquad FPUF \rightarrow Polyol + Gas_1$$

$$(2) \qquad Polyol \rightarrow Residule + Gas_2.$$

In the first reaction, virgin $FPUF$ decomposes into an intermediate product called $Polyol$, and pyrolyzate gas as referred as to Gas_1. Then, in the second reaction, $Polyol$ continues to decompose producing $Residule$ and Gas_2. These reactions were used to obtain the kinetic parameters, defined by a pre-exponential factor (A), activation energy (E_a), and stochiometric coefficients of the reactions. To acquire these parameters, TGA experiments were conducted at 10 K min^{-1}, and the ThermaKin model was used to inversely analyze the experimental data. The results obtained are shown in Table 4.1.

Table 4.1. Reaction kinetics parameters optimized from TGA model.

Reaction #	A (s^{-1})	E_a (kJ mol^{-1})	Stoichiometry
1	2.45×10^{13}	168	$FPUF \rightarrow 0.733\ Polyol + 0.267\ Gas_1$
2	5.59×10^{18}	262	$Polyol \rightarrow 0.033\ Residule + 0.967\ Gas_2$

Using kinetic parameters determined from the TGA model, the ThemaKin model was optimized using 10 K min^{-1} DSC experimental data. The thermodynamics parameters including the heat capacity (c_p) and the heat of reaction for each decomposition (ΔH_r) were found, and are shown in Table 4.2 and 4.3, respectively.

Table 4.2. Heat capacities and heat of condensed phased components.

Component	c_p (J kg^{-1} K^{-1})
$FPUF$	2250
$Polyol$	2250
$Residual$	2000

Table 4.3. Heat of reaction obtained from thermal decomposition of FPUF.

Reaction	ΔH_r (J kg^{-1})
$FPUF \rightarrow Polyol + Gas_1$	168
$Polyol \rightarrow Residule + Gas_2$	262

Lastly, the heat of combustion (ΔH_c) of the gaseous products of thermal decomposition was obtained by simulating MCC experiments at a nominal heating rate of 10 K min^{-1}, along with the reaction kinetics determined by the TGA. ΔH_c of both pyrolyze gas species, Gas_1 and Gas_2, were found the be 28×10^3 J kg^{-1} [22]. All of the decomposition model parameters were then used to further develop the thermal transport properties through an inverse analysis using CAPA experiment data.

4.1.2 CAPA Model Boundary Conditions

The experimental results of CAPA II in the anaerobic atmosphere were used to model a one-dimensional ThermaKin2Ds simulation. This simulation mode was defined by the experimental top and bottom boundary conditions.

4.1.2.1 Top Boundary

The top boundary of the CAPA model was defined by radiative ($q_{r,top}$) and convective ($q_{c,top}$) heat fluxes. However, FPUF samples in the CAPA experiments showed unique physical decomposition behavior, collapsing to the bottom of the sample holder in a relatively short period. In the CAPA II experiment, the samples were positioned 7 mm above the sample holder, as detailed in Section 2.2.1. The ThermaKin model can accurately predict any increase in heat flux due to the sample surface being higher than the setpoint level. However, the model cannot accurately predict any heat flux reduction due to the sample surface being lower than the setpoint level. To address this unique behavior of the FPUF sample, $q_{r,top}$ was prescribed based on the experimentally observed time of each flux exposure. The radiative heat flux of the top boundary in CAPA model was prescribed as shown in Figure 4.1. The radiative heat flux was initially configured as a constant flux corresponding to the nominal conical radiant heater setting of each experiment (HF_s in Figure 4.1). Once the sample collapsed to the sample holder lip (setpoint level), the radiative heat flux was prescribed as a linear downward ramp until the samples fully collapsed into the pool, Afterward, a reduced heat flux remained constant, HF_b, in Figure 4.1, for the remainder of the simulation. The reduced heat flux was measured and found to be 8.5% of the setpoint flux setting.

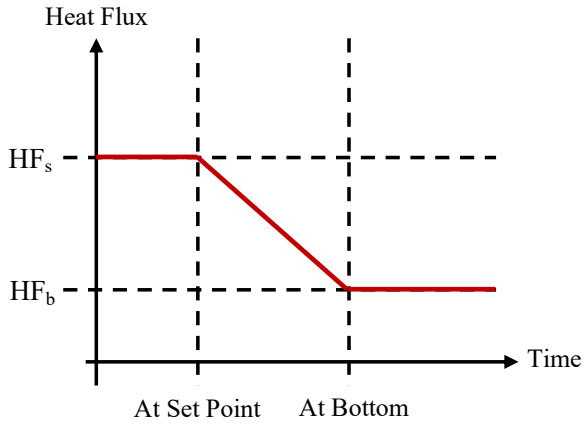

Figure 4.1. Prescribed radiative heat flux of top boundary CAPA model.

The convective heat flux of the top boundary ($q_{c,top}$) in ThermaKin was calculated by using the environmental temperature around the sample's top surface during the experiments ($T_{gas,top}$) and the convective heat transfer coefficient ($h_{c,top}$), which was found to be radically dependent as detailed in the previous study [24]. During the CAPA experiments, the environmental temperature was usually measured by the thermocouple located above the glass beads in the gas flow direction. The prescribed environmental temperature profile used in the ThermaKin model is

$$T_{gas,top} = C_1 e^{C_2 t} + C_3 e^{C_4 t} + T_{HFG} \quad (4.1)$$

where C_1, C_2, C_3, and C_4 are coefficients for the best experimental fit, T_{HFG} is the water temperature that is used to cool the heat flux gauge in K, and t is time in seconds. However, the thermocouple that was used to measure experimental $T_{gas,top}$ was often contaminated due to its location, resulting in an inaccurate measurement of $T_{gas,top}$. Alternatively, $T_{gas,top}$ of two heat fluxes, 25 and 60 kW m^{-2}, were measured, and the coefficients were obtained by fitting the $T_{gas,top}$. In this study, $T_{gas,top}$ was determined using linearly interpolated coefficients between the two heat fluxes' coefficients. The

experimental gas temperature coefficients of each nominal radiant heat flux are shown in Table 4.4, and $T_{gas,top}$ profiles of each flux along with the measured flux profiles are shown in Figure 4.2.

Table 4.4. Environmental gas temperature coefficients for CAPA model.

Nominal Heat Flux (kW m^{-2})	C_1 (K)	C_2 (K s^{-1})	C_1 (K)	C_4 (K s^{-1})	T_{HFG} (K)
26	51.1	8.0×10^{-6}	-33.4	-1.5×10^{-2}	290
41	79.8	8.7×10^{-6}	-51.2	-1.4×10^{-2}	290
62	117.9	9.5×10^{-6}	-74.9	-1.3×10^{-2}	290

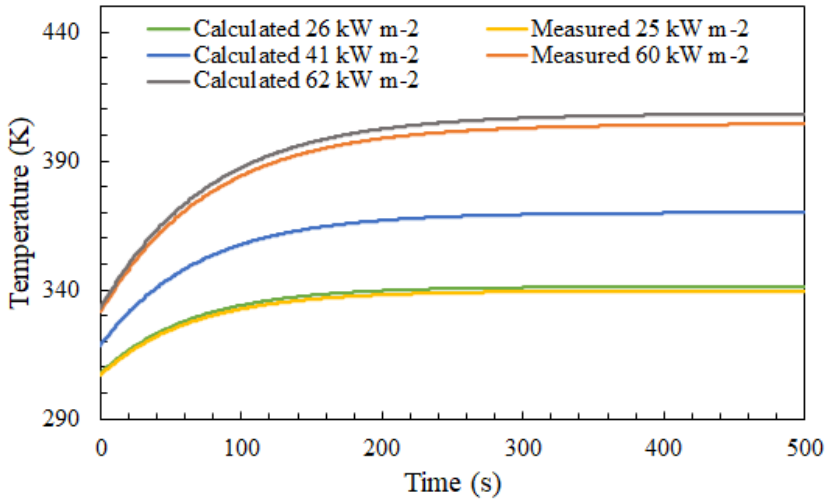

Figure 4.2. Environmental gas temperature profile of the sample top surface in each flux with fitted measurement flux profiles.

Once the $T_{gas,top}$ profile was established, the convective heat flux at the top boundary used in the ThermaKin model was calculated as

$$q_{c,top} = h_{c,top}(T_{gas,top} - T_{top}) \quad (4.2)$$

where T_{top} is the material top surface temperature in K.

4.1.2.2 Bottom Boundary

Similarly, to the top boundary, the bottom boundary of the CAPA model was also defined by the radiative ($q_{r,bottom}$) and convective ($q_{c,bottom}$) heat flux as

$$q_{r,bottom} = \varepsilon\sigma\left(T_{gas,bottom}^4 - T_{bottom}^4\right) \quad (4.3),$$

$$q_{c,bottom} = h_{c,bottom}\left(T_{gas,bottom}^4 - T_{bottom}^4\right) \quad (4.4),$$

where T_{bottom} is the temperature of the bottom surface of the sample, ε is the emissivity of the paint used on the copper foil at the bottom of the samples, σ is the Stefan-Boltzmann constant, $h_{c,bottom}$ is the average convective heat transfer coefficient of the bottom surface, found to be 4 W m^{-2} K^{-1} as detailed in the previous CAPA II study [24]. In equations 4.3 and 4.4, $T_{gas,bottom}$ represents the environmental temperature surrounding the bottom surface of the sample. This gas temperature was assumed to be equal to the temperature of the inner wall of the aluminum tube inside the CAPA II apparatus. For simplicity, the $T_{gas,bottom}$ profile used in ThemaKin model prescribed as a linear ramp up followed by a constant for the rest of the simulation. Figure 4.2 shows the experimental bottom surface temperature and fitted model. The fitted model includes the initial ($T_{gas,bottom,int}$) and final ($T_{gas,bottom,final}$) temperatures, as well as the model crossover time, which are summarized in Table 4.5.

Table 4.5. Summarized $T_{gas,bottom}$ with the crossover Time.

Nominal Heat Flux (kW m^{-2})	$\boldsymbol{T_{gas,bottom,int}}$ **(K)**	$\boldsymbol{T_{gas,bottom,final}}$ **(K)**	**Crossover Time (s)**
26	302	325.5	340
41	303	326.5	340
62	303	329	293

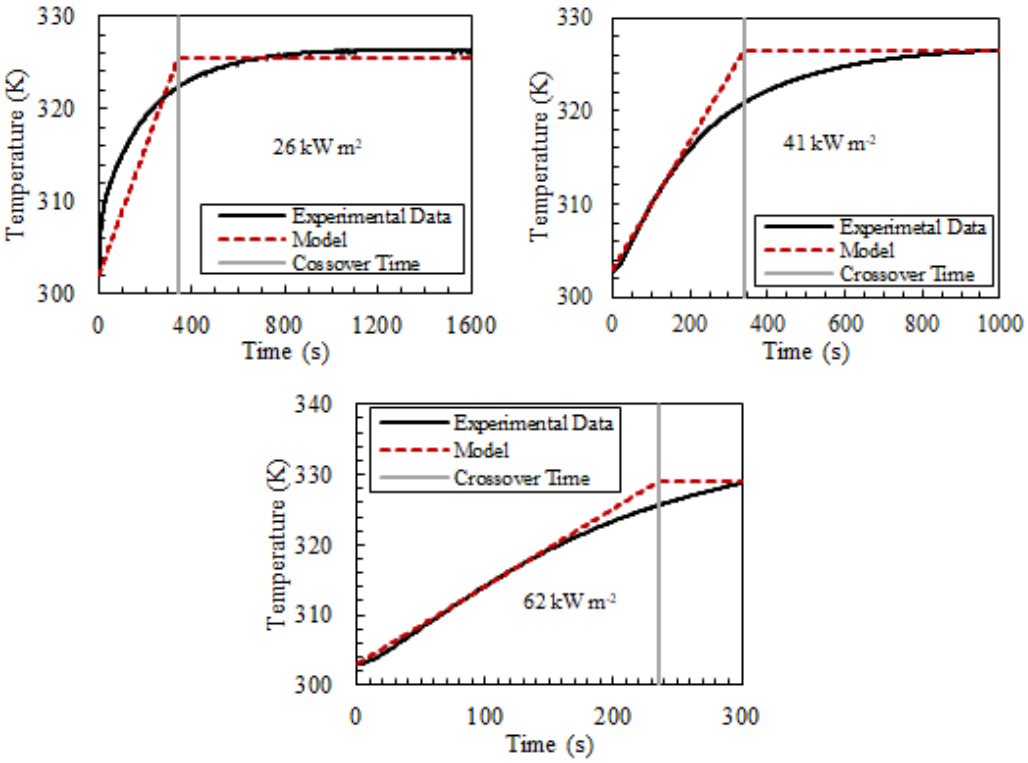

Figure 4.3. Experimental and fitted model of anaerobic atmospheric $T_{gas,bottom}$ for each nominal heat flux exposure.

4.1.2.3 Additional Model Assumptions

The optical properties of FFUF, including emissivity (ε) and absorption coefficient (α), used in the ThermaKin model were assumed based on literature values. Since the emissivity of virgin FPUF is unknown, it was assumed to be an average of common polymers in a fire-like environment, as measured by Linteris et al. [34] and found to be 0.92. To simplify, the emissivity of FPUF was assigned to be 0.9. The absorption coefficient used in the ThermaKin model was normalized by the FPUF density and set to 200 m^2 kg^{-1}, This value indicates that the sample absorbed all radiation only at the surface, with no in-depth absorption. Increasing this absorption coefficient would not affect the simulation results. There was limited information

available about the optical properties of the decomposition products of FPUF in the literature. Therefore, ε and α of all decomposition products were assumed to be equal to virgin FPUF and assigned to be 0.9 and 200 m2 kg^{-1}, respectively. The gas-phase components were initially assumed to be transparent to thermal radiation.

In this model, it was assumed that all gaseous decomposition products did not contribute to the volume of the sample [24]. The c_p of all gaseous decomposition products was 2100 J $Kg^{-1}K^{-1}$, based on an average c_p of collection of C1 – C8 hydrocarbon at 600 K [35]. The density of Polyol was measured to be 700 kg m^{-3} in a previous FPUF study [22].

4.2 Model Results

The initial approach of the simulation aimed to optimize a combination of the thermal conductivity of virgin FPUF (k_{FPUF}) and condensed-phase decomposition products (k_{prod}), which were set to be equal for both Polyol and FPUF residual, to achieve the best agreement between the model and experimental data. The optimization was explored in a wide range, with k_{FPUF} ranging from 0.04 - 0.1 W $m^{-1}K^{-1}$, and k_{prod} ranging from 1 - 3000 W $m^{-1}K^{-1}$. Note that for simplicity, the thermal conductivity of gaseous decomposition products (k_{gas}) are both assumed to be equal to k_{FPUF}.

The results of this initial approach did not accurately capture the physical behavior observed in the experiments, with both MLR and T_{bottom} being significantly overpredicted for all fluxes. Although this approach did not provide an adequate fit, the best agreement was found with a combination of k_{FPUF} and k_{prod} equal to 0.07 W $m^{-1}K^{-1}$ and 300 W $m^{-1}K^{-1}$, respectively, as shown in Figure 4.4.

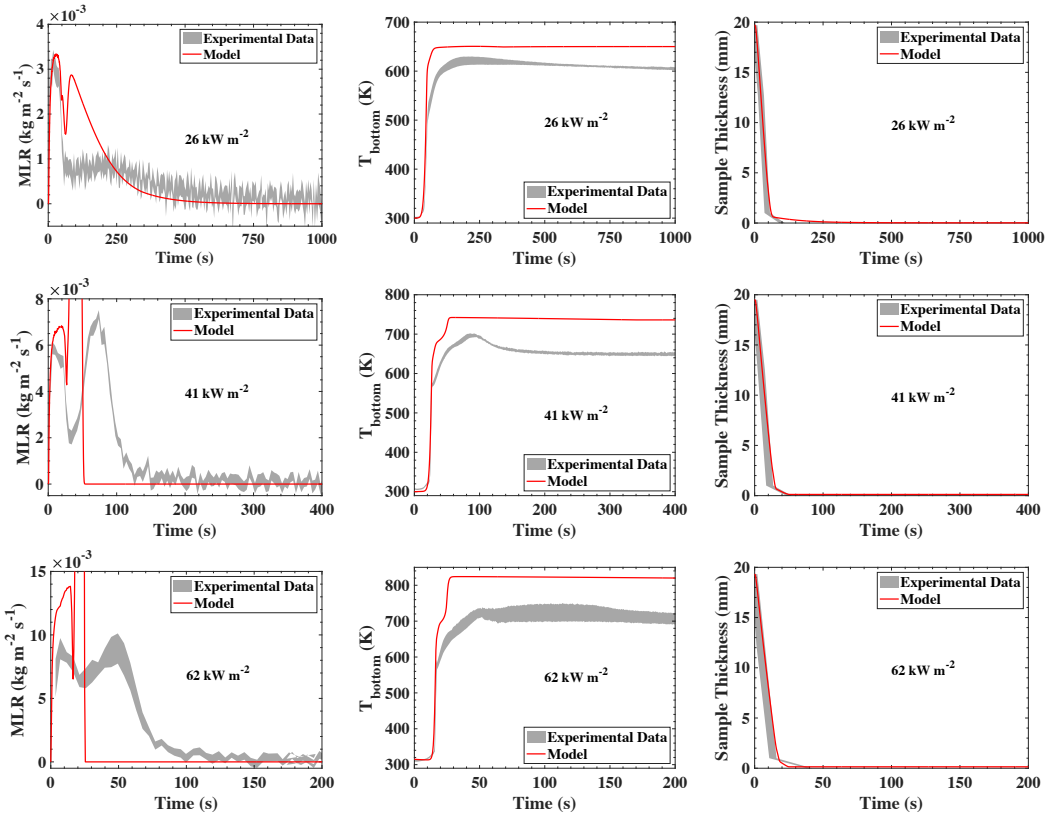

Figure 4.4. Experimental vs. modeled of anaerobic atmospheric CAPA MLR (left), T_{bottom} (middle), and sample thickness (right) for the first approach.

This best agreement was chosen based on visual observation between the model and experimental data along with optimized errors for both MLR and T_{bottom}, as defined in equations 4.5 and 4.6.

$$MLR_{err} = \frac{1}{N}\sum_{i=1}^{i=N}\left[\frac{1}{n\ MLR_{max}^{exp}}\sum_{j=1}^{j=n}\left|MLR_j^{exp} - MLR_j^{sim}\right|\right] \quad (4.5)$$

$$T_{b,err} = \frac{1}{N}\sum_{i=1}^{i=N}\left[\frac{1}{n\ T_{b,max}^{exp}}\sum_{j=1}^{j=n}\left|T_{b,j}^{exp} - T_{b,j}^{sim}\right|\right] \quad (4.6)$$

where

- n is the total number of compared points in each flux
- N is the number of simulated fluxes, which equals 3 (26, 41, and 62 kW m^{-2})
- MLR_j^{exp} and $T_{b,j}^{exp}$ are the experimental MLR and T_{bottom}, respectively

- MLR_j^{sim} and $T_{b,j}^{sim}$ are the simulation MLR and T_{bottom}, respectively
- MLR_{max}^{exp} and $T_{b,max}^{exp}$ are the maximum MLR and T_{bottom} of experimental data, respectively.

The optimized errors in equations 4.5 and 4.6 were used to calculate the total error of all fluxes between the simulation and experimental. A smaller total error indicates a closer match between the simulation model and the experimental data. Since MLR_{err} and $T_{b,err}$ were obtained separately, both errors must be compromised to achieve the best agreement for the model.

As observed and described in section 3.1.1, the physical decomposition behavior of FPUF involved the sample collapsing relatively quickly after exposure to radiant heat, while simultaneously forming bubbles on top of the surface as demonstrated in Figure 4.5. This bubbling/frothing, which was characterized by high absorptivity due to gas pockets within the bubbles, effectively reduced the radiant heat flux reaching the underlying pool of FPUF.

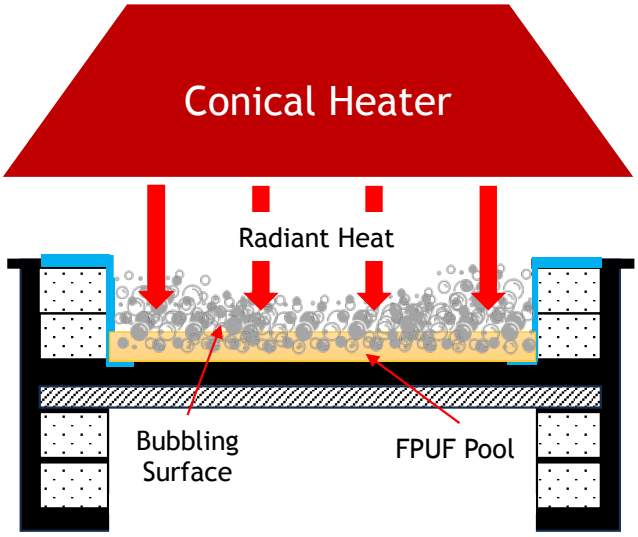

Figure 4.5. Graphical bubbling/frothing sample surface during radiant heat exposure.

To account for this phenomenon, a modified Beer-Lambert Law [36] was implemented as

$$\frac{HF_f}{HF_b} = e^{-c_x \overline{MLR}} \quad (4.7),$$

where

- HF_f is the final heat flux delivered to the pool underneath the bubbles,
- HF_b is the reduced heat flux measured in section 3.1.1 (~8.5 % of the nominal heat flux),
- $\overline{MLR}$ is an average MLR that is assumed to be approximately equal to the average concentration of absorbing material,
- c_x is an effective absorption coefficient.

Since the reduced heat flux of the front boundary condition accounted for the lower position of the sample (described in section 4.1.2.1), this heat flux modification aimed to reduce the radiant heat flux as it penetrated through the bubbled surface layer. This modification eliminated the initial assumption that all gas-phase components were transparent to thermal radiation. The effective absorption coefficient, c_x, accounted for the reduction ratio relative to the concentration of the decomposition species, which was assumed to be equal to the MLR of FPUF during its decomposition process. To simplify the calculation, an average MLR ($\overline{MLR}$) was utilized and obtained from the CAPA experimental MLR of each flux. Because FPUF decomposed very quickly during the experiment, most of the significant MLR occurred at the beginning of the experiments. Therefore, $\overline{MLR}$ was calculated from the beginning of the experiment until the second peak was reduced to 30% of its peak value. Figure 4.5 illustrates the

region of experimental MLR where $\overline{MLR}$ was calculated, and the values are shown in Table 4.6.

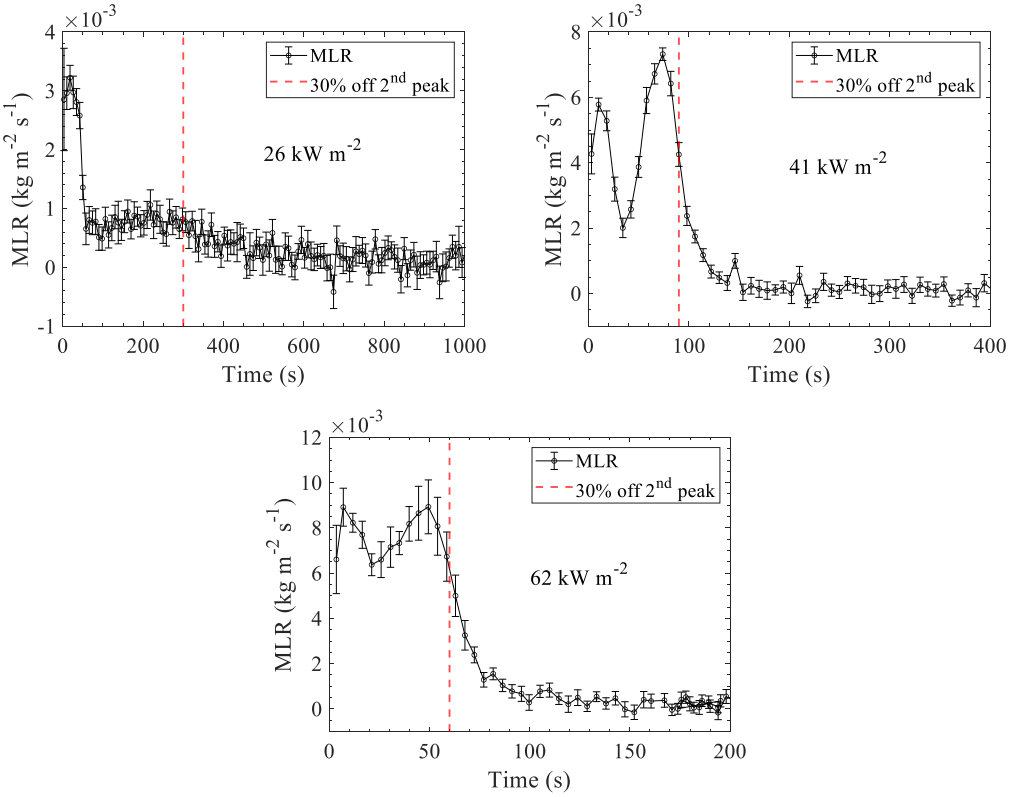

Figure 4.6. Anaerobic atmospheric CAPA experimental MLR with the 30% off 2nd peak for each heat flux exposure.

Table 4.6. $\overline{MLR}$ used for heat flux reduction CAPA model.

Nominal Heat Flux ($kW\ m^{-2}$)	**30% off Peak Time** (s)	$\overline{MLR}$ ($kg\ m^{-2}\ s^{-1}$)
26	300	1.12×10^{-3}
41	90	4.86×10^{-3}
62	60	7.65×10^{-3}

In this approach, the Thermakin model was optimized by exploring a combination of k_{FPUF}, k_{prod}, and c_x. The optimization range for both conductivities remained the same as the first approach: k_{FPUF} ranged from 0.04 - 0.1 $W\ m^{-1}K^{-1}$ and

k_{prod} ranged from 1 – 3000 W $m^{-1}K^{-1}$. The parameter c_x ranged from 0 - 120 m^2s kg^{-1} (with c_x equal to 0 m^2s kg^{-1} in the first approach). The best agreement between the model and simulation was determined using the same criteria as the first approach, which involved visual observation and optimized errors from equations 4.5 - 4.6. As a result, the optimal values found were k_{FPUF}, k_{prod} and c_x assigned to 0.07 W $m^{-1}K^{-1}$, 200 W $m^{-1}K^{-1}$, and 80 m^2s kg^{-1}, respectively. The simulation results of MLR and T_{bottom} of each heat flux are shown in Figure 4.7.

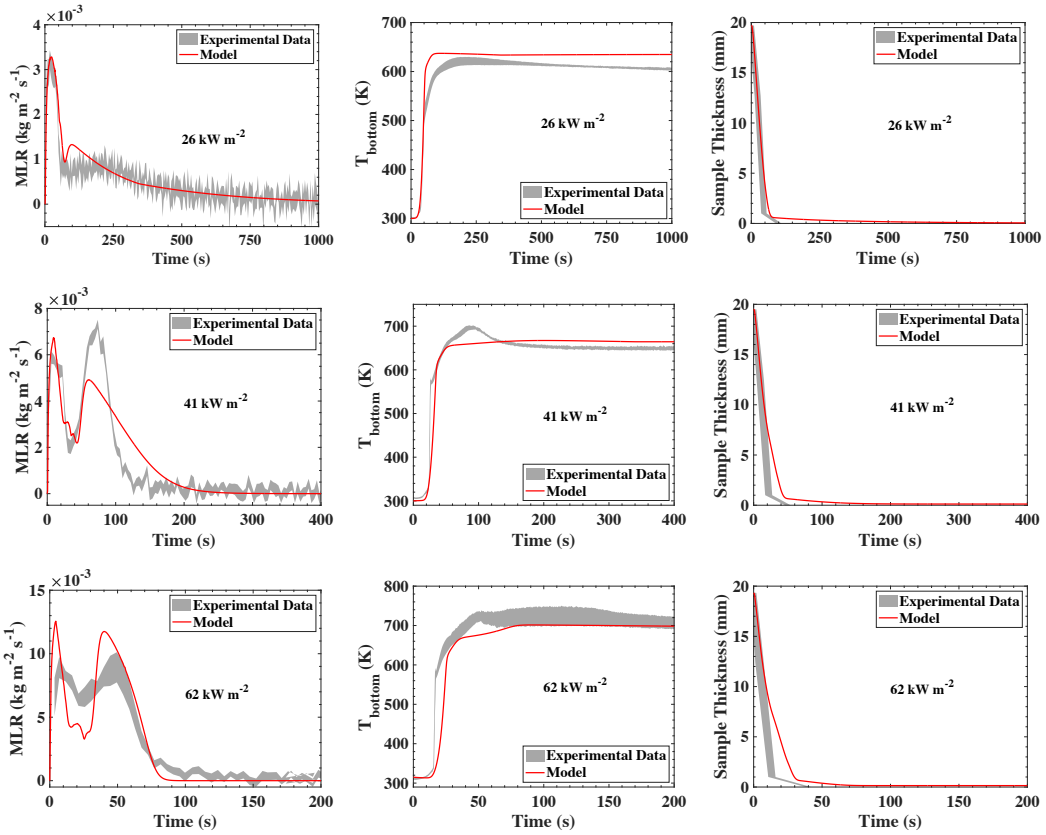

Figure 4.7. Experimental vs. modeled of anaerobic atmospheric CAPA MLR (Left) and T_{bottom} (right) of the effective absorption coefficient approach at all heat flux exposure.

With this combination of all parameters, the modeled MLR and T_{bottom} closely resembled the experimental behavior at all three fluxes. The modeled T_{bottom}

accommodated all fluxes. While the model T_{bottom} at 26 kW m^{-2} was slightly overpredicted, and at 62 kW m^{-2} was slightly underpredicted, the T_{bottom} of 41 kW m^{-2} was closely predicted. Similarly to the modeled MLR, the first peak of the modeled MLR at 26 kW m^{-2} and 41 kW m^{-2} was effectively captured the experimental data, but the second peak at 26 kW m^{-2} was overpredicted while at 41 kW m^{-2} was underpredicted. The modeled MLR of 60 kW m^{-2} was overpredicted at both peaks, but the timing of the peaks was MLR behavior was well captured. The sample thickness profile was also predicted by the model. The model accurately captured the timing of the foam collapse at 26 kW m^{-2}, but it was slightly delayed at 41 and 62 kW m^{-2} compared to the experimental observations. The optimized thermal conductivities of each component, along with other properties used in the CAPA model as shown in Table 4.7.

Table 4.7. Transport properties of each component used in the ThermaKin Modeling.

Component	Density (kg m^{-3})	Conductivity (k) (W m^{-1} K^{-1})	Emissivity (ε)	Absorption (α) (m^{-2} kg)
FPUF	29.40	0.07	0.9	200
Polyol	700	200	0.9	200
Residual	700	200	0.9	200

4.3 Model Validation

Cone calorimeter experimental data, with properties defined from the CAPA model, were used to compare with a cone calorimeter model. Note that the conditions of the cone calorimeter experiment were completely different from those of the CAPA experiments, particularly, with the presence of a flame presented in the cone experiment. In this regard, the heat flux delivered to the sample was a combination of

the set conical heater, and heat from the flame, which included both convective and radiative heat transfer modes. Because the parameter c_x accounted for radiative heat flux reduction due to the bubbling surface in the CAPA model, it was applied solely to the radiative heat flux portion of the cone calorimeter model for consistency between the two models.

To apply c_x in equation 4.7, The average MLR from the experiments was required. However, the MLR behavior from the experiments showed two distinct peaks, with the second peak occurring sometime after the first peak relative to the experimental duration. Unlike CAPA experimental MLR behavior, where two peaks occurred relatively close to each other. Consequently, $\overline{MLR}$ of each peak was obtained separately from 30% before and after its peak value, and the time between the peak was determined to be 20 s. Figure 4.8 shows the regions where $\overline{MLR}$s were calculated, and the values are shown in Table 4.8.

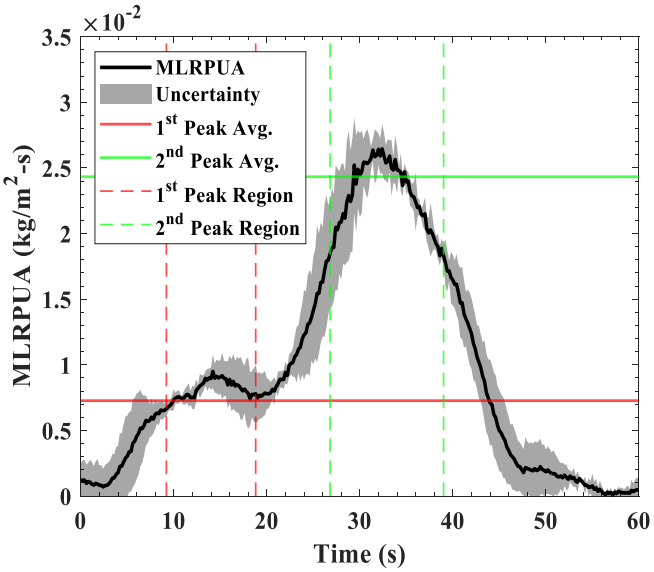

Figure 4.8. MLRPUA with the 30% off peak regions of the cone calorimeter experiments at 26 kW m^{-2} heat flux exposure.

Table 4.8. $\overline{MLR}$ with the corresponding time of cone calorimeter MLR.

Peak #	$\overline{MLR}$ (kg m^{-2} s^{-1})	30% off Peak Time (s)
1	7.3×10^{-3}	9 - 19
2	24.3×10^{-3}	27 - 39

By applying the reduction of radiative heat flux to the cone calorimeter model the front boundary radiative heat flux of the cone ($q_{r,cone}$) was prescribed as a steps function as shown in Figure 4.9. Initially, $q_{r,cone}$ was held constant at the nominal heat flux set on the conical heater (26 kW m^{-2}) until ignition occurred (~ 3.5 s), at which point the foam received heat from both the flame and conical heater. After the foam was ignited, $q_{r,cone}$, which represented the total radiative heat flux delivered to the foam, was reduced using the first peak $\overline{MLR}$, and remained constant until 20 s, when $\overline{MLR}$ peaks were split. Then, $q_{r,cone}$ was reduced, once again, using the second peak $\overline{MLR}$, and held constant for the remaining simulation.

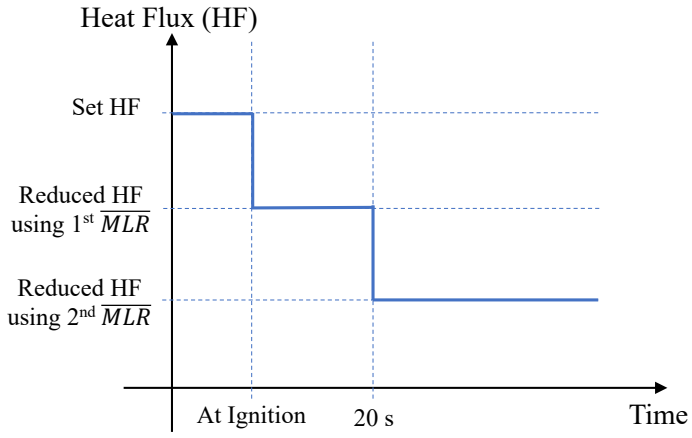

Figure 4.9. Prescribed radiative heat flux for front boundary of the cone calorimeter model.

The comparison between experimental data and the simulation model of the cone calorimeter is shown in Figure 4.10. The comparison indicates that the simulation

of the model accurately captured the ignition time observed in the experiment. However, the peak experimental HRRPUA was overpredicted by the model, resulting in an early extinction of the flame in the simulation. This discrepancy between the model and the experiments is potentially due to the assumption made to account for the bubbling surface of the foam, which reduced only radiative heat flux while ignoring the reduction of convective heat flux from the flame. The convective heat flux is the dominant mode of heat transfer from the flame to the pyrolyzing foam in a cone calorimeter [31]. Aside from the overprediction, the overall behavior observed in the experiments was fairly well captured by the simulation.

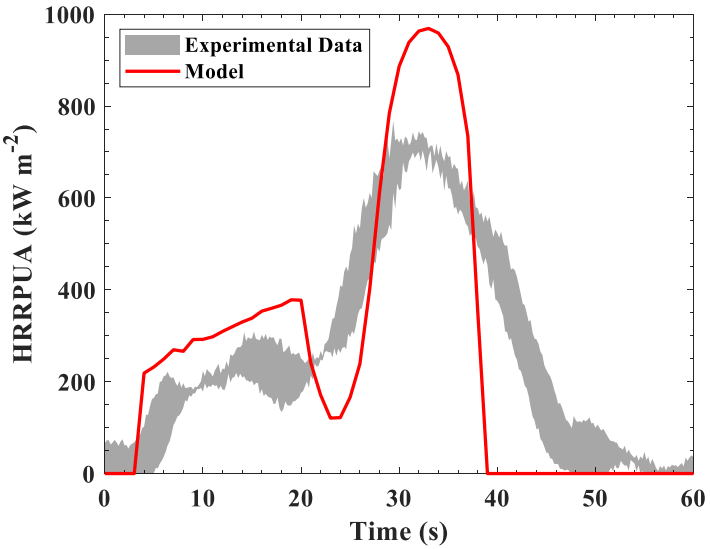

Figure 4.10. The comparison of experimental data and the simulation model of cone calorimeter at 26 kW m^{-2} exposure.

Chapter 5: Conclusion and Future Work

CAPA II Experiments were performed on NIST standard FPUF to determine thermal transport properties and develop a complete pyrolysis model in an anaerobic atmosphere. The parameter sets in the model were developed using a hierarchical approach [10] and validated against the experimental results of the cone calorimeter. An accurate thermal decomposition model developed in a previous study by Saar [22] was adopted to complete the model. ThermaKin2Ds was utilized to perform an inverse analysis of CAPA II experimental data, resulting in the thermal transport properties of FPUF including thermal conductivity and density of condensed-phase components. An effective absorption coefficient was implemented in CAPA modeling to correct for the reduction of radiant heat flux delivered to the foam due to the bubbling surface of the foam. As a result, the thermal transport properties were found to be reasonable for capturing both the CAPA II and the cone calorimeter experimental behavior. However, the optical properties of the FPUF decomposition products could not be measured directly and had to be assumed, which reduces the accuracy of the presented model. It is recommended that future study focuses on these properties, as they may improve the accuracy of the model and enhance the prediction of the fire simulation.

Furthermore, the reduction in radiative heat flux of the cone calorimeter model was calculated using the same effective absorption coefficient as in the CAPA model. However, in the cone calorimeter experiments, the sample was primarily exposed to the convective heat flux from the flame. The model assumed that the bubbling surface of the foam did not reduce this dominant convective heat flux. It is recommended that future studies further investigate the reduction of both radiative and convective heat

fluxes due to the unique behavior of FPUF during the decomposition in the cone calorimeter experiments.

Appendices

A1. Sample Holder Preparation for CAPA II Experiment

The procedures for the sample holder preparation are as follows:

1) Cut four insulation rings using 6.35 mm (1/4") thick Kaowool PM with an inside diameter of 70 mm (Total of 4 rings)
2) Place two layers of insulation rings at the bottom of the sample holder
3) Place painted aluminum mesh and copper foil on top of the rings
4) Place another two of the insulation rings on the foil
5) Cut the insulation tape into 25 mm long strips
6) Place the strips from the foil (~ 1 mm on the foil) to the lip of the sample holder
7) Place the next strip about 1 mm overlapping the previous strip
8) Repeat applying the tape strips around the holder until the insulation rings are fully covered with tape.

Figure A1.1. shows the drawing of the sample holder configuration and the sample in the sample holder. Figure A1.2. shows the sample holder photos.

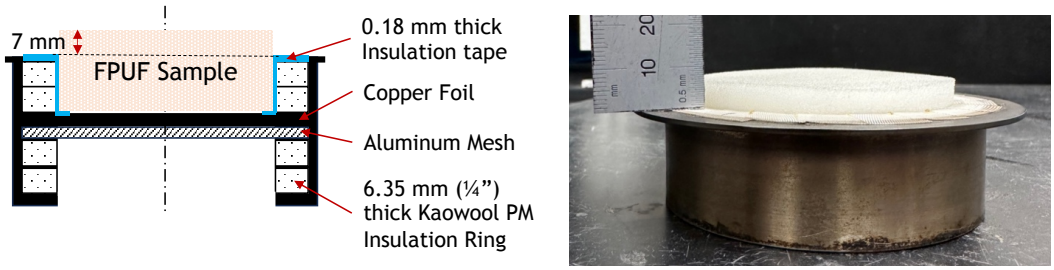

Figure A1.1. Sample holder drawing and its configuration (left) and sample holder with sample inserted (right).

Figure A1.2. Sample holder for FPUF samples used in CAPA II experiment.

References

[1] Shelby Hall, “Home Structure Fires,” National Fire Protection Association (NFPA). Accessed: Aug. 05, 2024. [Online]. Available: https://www.nfpa.org/education-and-research/research/nfpa-research/fire-statistical-reports/home-structure-fires

[2] M. Ahrens and R. Maheshwari, “Home Structure Fires Supporting Tables (NFPA®),” Oct. 2021.

[3] “InTouch1.1.” Accessed: Jul. 14, 2024. [Online]. Available: https://www.pfa.org/wp-content/uploads/2019/02/IntouchV1.1a.pdf

[4] A. B. Morgan, “Revisiting flexible polyurethane foam flammability in furniture and bedding in the United States,” *Fire Mater*, vol. 45, no. 1, pp. 68–80, Jan. 2021, doi: 10.1002/fam.2848.

[5] State of California Department of Consumer Affairs, “Requirements, Test Procedure and Apparatus for Testing the Smolder Resistance of Materials Used in Upholstered Furniture,” 2013.

[6] UNITED STATES CONSUMER PRODUCT SAFETY COMMISSION, “LABORATORY TEAT MANUAL For 16 C.F.R. Part 1632: Standard for the Flammability of Mattresses and Mattress Pads.” Accessed: Jul. 23, 2024. [Online]. Available: https://www.cpsc.gov/s3fs-public/pdfs/blk_media_testmatt.pdf

[7] UNITED STATES CONSUMER PRODUCT SAFETY COMMISSION, “LABORATORY TEST MANUAL FOR 16 CFR Part 1633: Standard for the Flammability (Open Flame) of Mattress Sets,” 2011. Accessed: Jul. 23, 2024. [Online]. Available: https://www.cpsc.gov/s3fs-public/pdfs/blk_media_labmanual.pdf

[8] I. Kim *et al.*, “Demonstration of an all-in-one solution for fire safe upholstery furniture: A benign backcoating for smoldering and flame-resistant cover fabrics,” *Fire Mater*, vol. 46, no. 4, pp. 677–693, Jun. 2022, doi: 10.1002/fam.3015.

[9] G. Di Cristina, R. Falkenstein-Smith, I. Kim, S. Wessies, M. Bundy, and M. Zammarano, “Towards fire safe and flame-retardant-free upholstered furniture,” *Proceedings of the Combustion Institute*, vol. 40, no. 1–4, p. 105399, 2024, doi: 10.1016/j.proci.2024.105399.

[10] S. I. Stoliarov and Y. Ding, “Pyrolysis model parameterization and fire growth prediction: The state of the art,” *Fire Saf J*, vol. 140, p. 103905, Oct. 2023, doi: 10.1016/j.firesaf.2023.103905.

[11] J. B. Henderson, J. A. Wiebelt, and M. R. Tant, “A Model for the Thermal Response of Polymer Composite Materials with Experimental Verification,” *J Compos Mater*, vol. 19, no. 6, pp. 579–595, Nov. 1985, doi: 10.1177/002199838501900608.

[12] Christian Vovelle, Jean-Louis Delfau, Marcelline Reuillon, Jacques Bransier, and Najib Laraqui, “Experimental and Numerical Study of the Thermal Degradation of PMMA,” *Combustion Science and Technology*, vol. 53, no. 2–3, pp. 187–201, Jun. 1987, doi: 10.1080/00102208708947026.

[13] C. Lautenberger and C. Fernandez-Pello, “Generalized pyrolysis model for combustible solids,” *Fire Saf J*, vol. 44, no. 6, pp. 819–839, Aug. 2009, doi: 10.1016/j.firesaf.2009.03.011.

[14] C. Lautenberger, “Gpyro3D: A Three Dimensional Generalized Pyrolysis Model,” *Fire Safety Science*, vol. 11, pp. 193–207, 2014, doi: 10.3801/IAFSS.FSS.11-193.

[15] K. B. McGrattan and G. P. Forney, “Fire dynamics simulator (version 4) :,” Gaithersburg, MD, 2004. doi: 10.6028/NIST.SP.1019.

[16] S. I. Stoliarov and R. E. Lyon, “Thermo-kinetic model of burning for pyrolyzing materials,” in *Fire Safety Science*, 2008, pp. 1141–1152. doi: 10.3801/IAFSS.FSS.9-1141.

[17] S. I. Stoliarov, I. T. Leventon, and R. E. Lyon, “Two-dimensional model of burning for pyrolyzable solids,” *Fire Mater*, vol. 38, no. 3, pp. 391–408, Apr. 2014, doi: 10.1002/fam.2187.

[18] T. J. Ohlemiller, “Modeling of smoldering combustion propagation,” *Prog Energy Combust Sci*, vol. 11, no. 4, pp. 277–310, Jan. 1985, doi: 10.1016/0360-1285(85)90004-8.

[19] D. S. W. Pau, C. M. Fleischmann, M. J. Spearpoint, and K. Y. Li, “Determination of kinetic properties of polyurethane foam decomposition for pyrolysis modelling,” *J Fire Sci*, vol. 31, no. 4, pp. 356–384, Jul. 2013, doi: 10.1177/0734904113475858.

[20] M. A. Garrido and R. Font, “Pyrolysis and combustion study of flexible polyurethane foam,” *J Anal Appl Pyrolysis*, vol. 113, pp. 202–215, May 2015, doi: 10.1016/j.jaap.2014.12.017.

[21] K. Prasad, R. Kramer, N. Marsh, M. Nyden, T. Ohlemiller, and M. Zammarano, “NUMERICAL SIMULATION OF FIRE SPREAD ON POLYURETHANE FOAM SLABS,” 2009.

[22] W. K. Saar, “DEVELOPMENT OF A COMPREHENSIVE PYROLYSIS MODEL FOR FLEXIBLE POLYURETHANE FOAM,” 2021. doi: https://doi.org/10.13016/dwwo-hmr2.

[23] ASTM 1354-17, “Standard Test Method for Heat and Visible Smoke Release Rates for Materials and Products Using an Oxygen Consumption Calorimeter,” 2017.

[24] J. D. Swann, Y. Ding, M. B. McKinnon, and S. I. Stoliarov, “Controlled atmosphere pyrolysis apparatus II (CAPA II): A new tool for analysis of pyrolysis of charring and intumescent polymers,” *Fire Saf J*, vol. 91, pp. 130–139, Jul. 2017, doi: 10.1016/j.firesaf.2017.03.038.

[25] J. Li and S. I. Stoliarov, “Measurement of kinetics and thermodynamics of the thermal degradation for non-charring polymers,” *Combust Flame*, vol. 160, no. 7, pp. 1287–1297, Jul. 2013, doi: 10.1016/j.combustflame.2013.02.012.

[26] J. Li and S. I. Stoliarov, “Measurement of kinetics and thermodynamics of the thermal degradation for charring polymers,” *Polym Degrad Stab*, vol. 106, pp. 2–15, Aug. 2014, doi: 10.1016/j.polymdegradstab.2013.09.022.

[27] M. McKinnon and S. Stoliarov, “Pyrolysis Model Development for a Multilayer Floor Covering,” *Materials*, vol. 8, no. 9, pp. 6117–6153, Sep. 2015, doi: 10.3390/ma8095295.

[28] J. Li, J. Gong, and S. I. Stoliarov, “Development of pyrolysis models for charring polymers,” *Polym Degrad Stab*, vol. 115, pp. 138–152, May 2015, doi: 10.1016/j.polymdegradstab.2015.03.003.

[29] Y. Ding, J. D. Swann, Q. Sun, S. I. Stoliarov, and R. H. Kraemer, “Development of a pyrolysis model for glass fiber reinforced polyamide 66 blended with red phosphorus: Relationship between flammability behavior and material composition,” *Compos B Eng*, vol. 176, p. 107263, Nov. 2019, doi: 10.1016/j.compositesb.2019.107263.

[30] J. D. Swann, Y. Ding, and S. I. Stoliarov, “Characterization of pyrolysis and combustion of rigid poly(vinyl chloride) using two-dimensional modeling,” *Int J Heat Mass Transf*, vol. 132, pp. 347–361, Apr. 2019, doi: 10.1016/j.ijheatmasstransfer.2018.12.011.

[31] C. G. McCoy, J. L. Tilles, and S. I. Stoliarov, “Empirical Model of flame heat feedback for simulation of cone calorimetry,” *Fire Saf J*, vol. 103, pp. 38–48, Jan. 2019, doi: 10.1016/j.firesaf.2018.11.006.

[32] O. Ugo-Okeke and D. Torvi, “Effects of incident heat flux on heat release rates and temperatures in cone calorimeter tests of polyurethane foam,” *Fire Mater*, 2024, doi: 10.1002/fam.3224.

[33] R. H. Krämer, M. Zammarano, G. T. Linteris, U. W. Gedde, and J. W. Gilman, "Heat release and structural collapse of flexible polyurethane foam," *Polym Degrad Stab*, vol. 95, no. 6, pp. 1115–1122, Jun. 2010, doi: 10.1016/j.polymdegradstab.2010.02.019.

[34] G. Linteris, M. Zammarano, B. Wilthan, and L. Hanssen, "Absorption and reflection of infrared radiation by polymers in fire-like environments," *Fire Mater*, vol. 36, no. 7, pp. 537–553, Nov. 2012, doi: 10.1002/fam.1113.

[35] P. J. Linstrom and W. G. Mallard, "The NIST Chemistry WebBook: A Chemical Data Resource on the Internet †", doi: 10.1021/je000236i.

[36] Theodore L. Bergman, Adrienne S. Lavine, Frank P. Incropera, and David P. DeWitt, *Fundamentals of Heat and Mass Transfer*, 6th Edition. 2020.